Noname manuscript No.
(will be inserted by the editor)

Phase-field modeling of fracture in ferroelectric materials

Amir Abdollahi · Irene Arias

Received: date / Accepted: date

Abstract This paper presents a family of phase-field models for the coupled simulation of the microstructure formation and evolution, and the nucleation and propagation of cracks in single and polycrystalline ferroelectric materials. The first objective is to introduce a phase-field model for ferroelectric single crystals. The model naturally couples two existing energetic phase-field approaches for brittle fracture and ferroelectric domain formation and evolution. Simulations show the interactions between the microstructure and the crack under mechanical and electromechanical loadings. Another objective of this paper is to encode different crack face boundary conditions into the phase-field framework since these conditions strongly affect the fracture behavior of ferroelectrics. The smeared imposition of these conditions are discussed and the results are compared with that of sharp crack models to validate the proposed approaches. Simulations show the effects of different conditions and electromechanical loadings on the crack propagation. In a third step, the model is modified by introducing a crack non-interpenetration condition in the variational approach to fracture accounting for the asymmetric behavior in tension and compression. The modified model makes it possible to explain anisotropic crack growth in ferroelectrics under the Vickers indentation loading. This model is also employed for the fracture analysis of multilayer ferroelectric actuators, which shows the potential of the model for future applications. The coupled phase-field model is also extended to polycrystals by introducing realistic polycrystalline microstructures in the model. Inter- and trans-granular crack propagation modes are observed in the simulations. Finally, and for completeness, the phase-field theory is extended to the simulation of the propagation of conducting cracks under purely electrical loading and to the three-dimensional simulation of crack propagation in ferroelectric single crystals. Salient features of the crack propagation phenomenon predicted by the simulations of this paper are directly compared with experimental observations.

Keywords Ferroelectricity · Piezoelectricity · Fracture · Phase-field models · Polycrystals · Finite element analysis · Domain switching

A. Abdollahi · I. Arias
Laboratori de Càlcul Numèric (LaCàN, Departament de Matemtica Aplicada III, Universitat Politècnica de Catalunya (UPC), Campus Nord UPC-C2, E-08034 Barcelona, Spain
E-mail: irene.arias@upc.edu

1 Introduction

Ferroelectric ceramics are important functional materials that are widely used for industrial applications such as sensors, actuators and transducers, thanks to their unique electromechanical coupling properties. However, their inherent brittleness is a major concern on their reliable operation in devices, which demands a deep understanding of the fracture behavior. Over the past decades, there have been substantial advances in both theoretical and experimental investigations on the fracture of ferroelectric ceramics. Excellent reviews of these works have been presented [59, 100, 140]. Due to the underlying microscopic mechanisms, ferroelectric ceramics exhibit ferroelectric and ferroelastic switching behavior with macroscopic dielectric and butterfly hystereses (See [46, 52, 63] for reviews on related modeling approaches). The formation and evolution of the microstructure are the main sources of non- linearity of ferroelectrics and are more probable in the vicinity of cracks due to the intensive fields [39, 51, 90]. Nonlinear

interactions between the microstructure and the localized stress and electric fields near the crack tip lead to the complexity of fracture in ferroelectric materials [12, 41, 93, 104]. Therefore, it is necessary to incorporate the microscopic phenomena into the analysis of the global reliability of ferroelectric components.

There are a number of theoretical approaches to the understanding of fracture phenomena in ferroelectric ceramics, which can be classified into three groups. The first group is based on the linear theory of piezoelectricity where microstructure effects are not taken into account. These models have been employed to study the basic concepts of the linear theory in the context of fracture mechanics and to evaluate the effects of individual and coupled electromechanical fields and different crack-face boundary conditions [62, 66, 77, 78]. As a development, the effect of remanent polarization has been considered in these models to obtain energy release rates in poled ferroelectrics [44]. The second group is related to more realistic approaches of ferroelectric materials which take into account the nonlinear microstructure effects. These include phenomenological models inspired in plasticity theory [61, 79, 104, 124] and small-scale switching models [12, 138, 147, 148], which rely on a simple local switching criterion [47]. These models are able to describe the local domain formation and phase transformation near the crack tip. The third group of theoretical approaches is based on phase-field or time-dependent Devonshire-Ginzburg-Landau (TDGL) models, which have been developed to explicitly describe the formation and evolution of individual ferroelectric domains in the framework of continuum mechanics [20, 102, 107, 110, 132, 135, 144]. These models have allowed researchers to study the nucleation and growth of domains near crack tips and the influence on the stress field [136], the mechanical and electromechanical $J-$integrals [64, 65, 108, 122, 125, 133], and nonlinear behavior of ferroelectrics [37]. For completeness, we mention that cohesive theories aimed at fracture in ferroelectric materials have also been proposed [10, 32].

Several experiments have been done to study the fracture behavior of ferroelectric ceramics. However, there are a number of contradictions and inconsistencies between reported results. Experiments on insulating cracks have shown that a positive electric field promotes crack extension perpendicular to the poling axis of the material, whereas a negative electric field retards it [75, 101, 112, 116]. Other tests have indicated an opposite phenomenon, where their results show that a positive applied electric field inhibits crack propagation, whereas crack propagation is enhanced under a negative applied electric field [50, 95, 106, 121]. On the other hand, experiments do not show a clear shielding or weakening effect of the microstructure on insulating cracks oriented parallel to the poling and electric field direction [112, 116]. This behavior is not expected since experiments without electric field indicate that in this configuration a pronounced domain switching zone is developed during crack growth [100]. Some experiments have been also performed to investigate the fracture mechanisms of electrically conducting cracks, where the electric field is applied parallel to the crack orientation and it is able to fracture ferroelectric specimens without additional mechanical load [30, 142]. However it is not understood why the electrical field intensity factors obtained in these works are four times larger than that of reported in other experiments [33, 45]. These contradictions and ambiguities confirm that the fracture of ferroelectric materials is a complex phenomenon and more sophisticated modeling approaches and experiments are required to create a sound basis of results for the understanding of the fracture behavior in these materials.

The above-mentioned models of ferroelectric fracture are useful to analyze the electromechanical fields near the tip of a fixed or stationary crack. However, these models are unable to study the crack propagation mechanisms, specially when the crack tip fields interact with the microstructure and obstacles such as defects or grain boundaries. There are a few theoretical attempts to study these mechanisms. Recently, phase-field models [69, 82, 130] and a strong discontinuity approach [96] have been proposed to simulate propagating cracks in linear piezoelectric solids, thus not accounting for the effect of ferroelectric domain microstructures. Towards more realistic approaches, we have proposed a family of coupled phase-field models for both the brittle crack propagation and the microstructure evolution by tackling the full complexity of the fracture phenomenon in ferroelectric materials [1, 2, 3, 4, 5, 6]. This paper extends the current state of the art in fracture of ferroelectric ceramics by reviewing these models and their developments which are outlined as follows:

1. *Coupled phase-field model.* A coupled phase-field model is presented based on two existing energetic phase-field approaches for brittle fracture and ferroelectric domain formation and evolution. Using this model, the interactions between the microstructure and the crack propagation are investigated in ferroelectric single crystals under mechanical and electromechanical loadings. See Section 3.

2. *Modeling of different crack-face boundary conditions.* Different electromechanical conditions, introduced as crack-face boundary conditions in sharp models, are encoded into the phase-field framework. The smeared imposition of these conditions are discussed and the results are compared with that of the sharp

crack models to validate the proposed approaches. Numerical simulations are performed to show the effects of different conditions and electromechanical loadings on the crack propagation. See Section 4.

3. *Phase-field simulation of anisotropic crack propagation.* The coupled phase-field model is developed by introducing a crack non-interpenetration condition in the variational approach to fracture accounting for the asymmetric behavior in tension and compression. The developed model makes it possible to explain anisotropic crack growth in ferroelectrics under the Vickers indentation loading. See Section 5.

4. *Crack initiation patterns at electrode edges in multilayer actuators.* The phase field model, introduced in Section 5, is employed for the fracture analysis of multilayer ferroelectric actuators. In particular, the objective of this section is to study the crack initiation at electrode edges during the poling process of the actuators. Considering different bonding conditions between the ceramic and electrode layers, different crack initiation patterns are obtained, which are useful to understand the fracture processes and to guide the design of this type of actuators. See Section 6.

5. *Inter- and trans-granular crack propagation in ferroelectric polycrystals.* The coupled phase-field model is extended to ferroelectric polycrystals. Different polycrystalline microstructures are obtained by implementing a computer simulation of grain growth model. By incorporating the differential fracture toughness of the bulk and the grain boundaries, and the different crystal orientations of the grains, the phase-field fracture model of ferroelectric single crystals is extended to polycrystals. Simulation results show intergranular crack propagation in fine-grain microstructures while transgranular crack propagation is observed in coarse grains. See Section 7.

6. *Conducting crack propagation driven by electric fields.* The aim of this section is to extend the phase-field theory to the simulation of conducting crack propagation and investigating the crack propagation mechanisms under purely electrical loading. This is done by introducing the electrical enthalpy of a diffuse conducting layer into the phase-field formulation. The results imply that the major driving force to propagate the conducting cracks is the electrostatic force due to the accumulation of charges with the same sign at the crack tip. See Section 8.

7. *Numerical simulation of 3-D crack propagation.* We present a three-dimensional simulation of crack propagation in ferroelectric single crystals. This is done by extending the phase-field model to three dimensions and running the simulation on a parallel machine. See Section 9.

The structure of this paper is as follows. The background information regarding ferroelectric materials and phase-field models is presented in Section 2. Sections 3 - 9 expand on the seven contributions mentioned above. The idea of these sections is to describe concisely the goals of the contribution, provide representative results and refer to the papers mentioned in each section for the details. The last section is the conclusion of the paper.

2 Background

2.1 Ferroelectric Materials

Ferroelectrics are a family of multi-phase crystalline materials with exceptional electromechanical properties. These materials are classified as a subcategory of piezoelectric materials, possessing dielectric hysteretic behavior. Applications for ferroelectric materials include sensors, capacitors, non-volatile memories, ultrasound imaging and actuators, electro-optic materials for data storage applications, thermistors, switches known as trans-chargers or trans-polarizers, oscillators and filters, light deflectors, modulators and displays [54, 70]. These materials possess a spontaneous electric polarization below a certain phase transition temperature, called the Curie temperature. This is due to dipoles formed by displacements of charged ions inside the crystal unit cell. Figure 1 presents the unit cell of ferroelectric lead titanate (PbTiO3) with a non-polar cubic symmetry above the Curie temperature. In the room temperature, the central atom of the unit cell (Ti) tends to one of the Oxygen atoms (O), hence stretching the cubic lattice along one of its lattice vectors. This atomic displacement produces a dipole per unit cell, and therefore a spontaneous electrical polarization. If the spontaneous polarization can be reversed by the application of an electric field opposite to its direction, these crystal structures are called ferroelectrics. The polarization can be oriented along six equivalent directions which give rise to six equivalent tetragonal phases in ferroelectrics presented in Fig. 2.

The application of a small mechanical or electrical load parallel to the polarization elongates the unit cell along the applied load and increases the polarization. In opposite, a small anti-parallel load results in a shrinkage of the unit cell and decreasing the polarization, see Fig. 3. In fact in response to a low applied mechanical load, a ferroelectric material will produce an electric charge proportional to the load. Similarly, the material will produce a mechanical deformation in response to a low applied electric field. These behaviors represent the

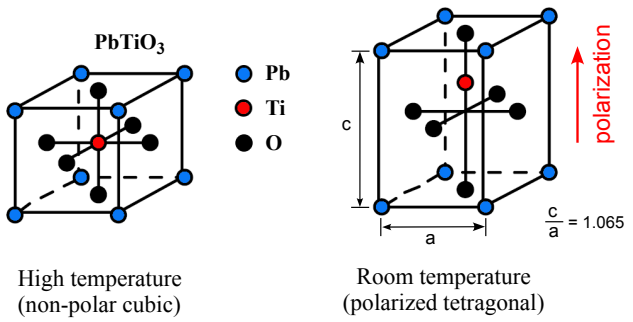

Fig. 1 Ferroelectric unit cell in (left) high temperature and (right) room temperature

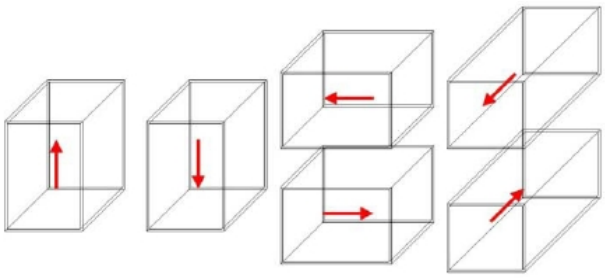

Fig. 2 Six equivalent tetragonal phases in ferroelectric crystals.

linear piezoelectric responses of ferroelectric materials under low electrical and mechanical loads.

By increasing the magnitude of the applied load opposite to the polarization, the unit cell is reoriented along other tetragonal phases to accommodate the large load. In the case of a large applied electric field, the polarization of the unit cell is reversed, parallel to the applied field. This polarization reorientation is called 180^o domain switching in ferroelectrics. On the other hand, a large compressive stress reorients the polarization by 90^o, along one of the adjacent tetragonal phases. This phenomenon is defined as 90^o ferroelastic domain switching, see Fig. 4.

A combination of the tetragonal phases forms a multi-domain structure of ferroelectric crystals. The boundary separating the phases is classified into 90^o and 180^o domain walls. Figure 5 presents a sample of the multi-domain structure in two dimensions. The application of an external mechanical or electrical load can rearrange this domain pattern through domain switching. In an unpoled ferroelectric material, the polarization of domains is random through the material and it is distributed in such way that the net macroscopic polarization is zero. By applying an electric field, the polarization of domains starts to align along the applied field. If the electric field is strong enough, the material shifts into the polar state. Figure 6 presents the net polarization as a function of the applied electric field. The transition from the unpoled state (point U) to the polar state (point A) is highlighted by the red curve. The point A shows a maximum polarization in the unit cell under a strong applied electric field. When the field is decreased, the polarization decreases and it reaches the remanent polarization $\mathbf{P_r}$ after removal of the electric field.

One consequence of the domain switching in ferroelectric materials is the occurrence of the ferroelectric hysteresis loop and butterfly hysteresis curve depicted

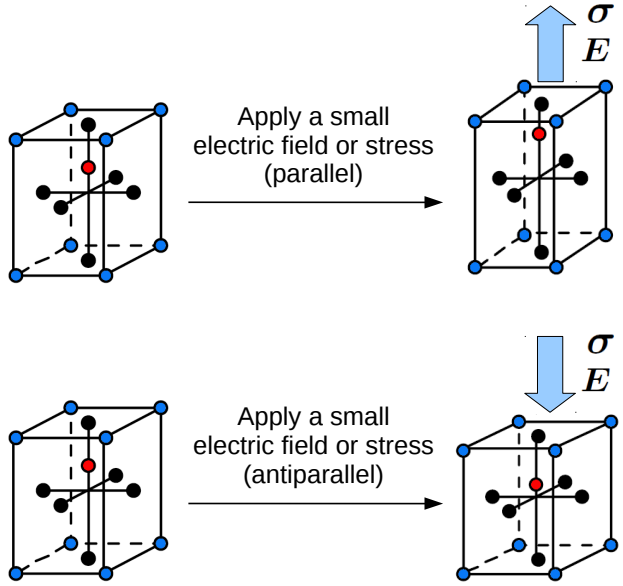

Fig. 3 Schematic of the ferroelectric until cell under a small electric field or stress: (top) parallel to the polarization, and (bottom) anti-parallel to the polarization .

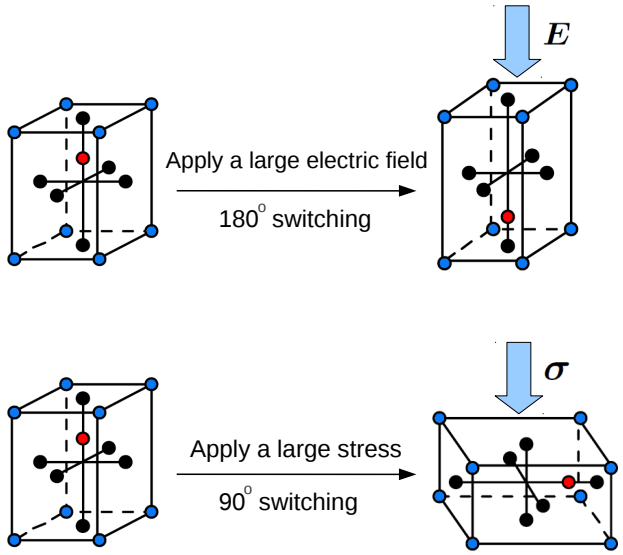

Fig. 4 Schematic of 180^0 ferroelectric and 90^0 ferroelastic switching at the unit cell level from large applied electric field and stress.

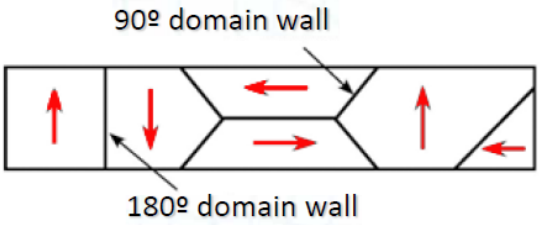

Fig. 5 A multi-domain ferroelectric structure in two dimensions.

in Fig. 6. When a negative electric field is applied (antiparallel to the polarization), the polarization decreases from the remanent value until a level where the polarization of some domains starts to reverse. A further increase of the field in the negative direction will cause the total reversal of the polarization. The polarization and strain responses in this region are strongly nonlinear. The field necessary to reverse the polarization is called the coercive field with the magnitude of $\mathbf{E_c}$. As the magnitude of the reverse field increases, the polarization reaches another maximum in the opposite direction (point -A). After that, if the field is again reversed, the polarization can be brought back to the previous maximum point depending on the field strength. Considerable changes of the polarization and strain under an alternative electric field are beneficial for many electromechanical applications.

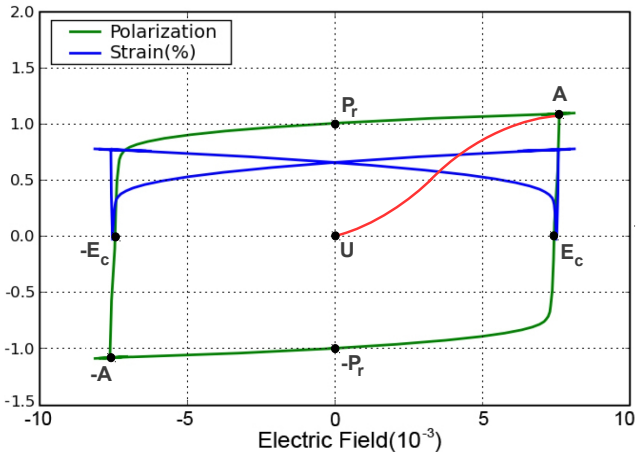

Fig. 6 Hysteresis loop (polarization-electric field) and butterfly hysteresis curve (strain-electric field) in poled ferroelectrics. The red curve indicates the transition from the unpoled state (point U) to the polar state (point A).

2.2 Phase-field models

Phase-field models are powerful tools to deal with moving interface problems [60]. Recently, phase-field models have gained a growing interest in physics and materials science, see [103, 109] and references therein. They are also employed in a wide range of applications in applied science and engineering such as fracture [28, 40, 83], growth of thin films [94] and grain structures [57], image segmentation [11], vesicle bio-membranes [88, 97, 126] and multi-phase flows [48], to mention a few. This paper also presents another application of phase-field models for microstructure formation and fracture evolution in ferroelectric materials [1, 2, 3, 4, 5, 6].

The idea behind phase-field modeling is to replace the sharp description of the interface by a smeared continuous layer. For this purpose, an auxiliary field, called order parameter or phase-field variable, is introduced to represent the phases (e.g. inside and outside of the crack), and also the interface. The phase-field variable adopts distinct values, say 0 and 1, in each of the phases, and smoothly varies between these values in the diffuse interface, see Fig. 7. This approach is also called diffuse-interface modeling.

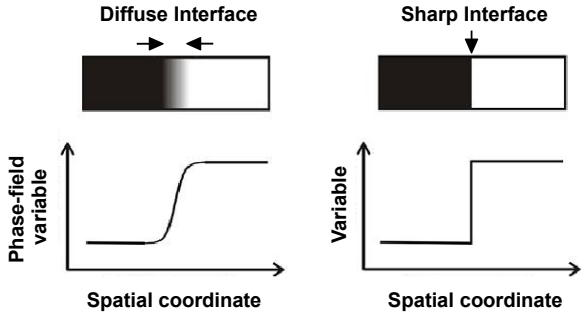

Fig. 7 Illustration of a (left) diffuse and (right) sharp interface.

Phase-field models are typically defined by an energy functional associated with different energy terms based on the physics of the problem. A general energy function E for these models can be constructed as

$$E[\boldsymbol{\eta}, \boldsymbol{\vartheta}] = F_1(\nabla \boldsymbol{\eta}) + F_{11}[\boldsymbol{\eta}, \boldsymbol{\vartheta}], \tag{1}$$

where $\boldsymbol{\eta}$ is the order parameter and $\boldsymbol{\vartheta}$ represents a set of physical variables in the problem under consideration. The function F_1 is the common energy term in the phase-field models associated with the gradient of the order parameter. This function penalizes sharp variations in the order parameter, hence introducing the interfacial energy between the phases. A positive regularization constant regulates the size of the interface in this

energy term. The function F_{11} characterizes the physical properties of the phases and it is associated with the order and physical parameters of the problem. In general, this energy furnishes a multi-well energy landscape with respect to the order parameter $\boldsymbol{\eta}$ with minima corresponding to the phases. Figure 8 presents a schematic of this energy landscape where m indicates the number of phases. This number can be as high as 100 in the model of grain growth in polycrystalline materials [57].

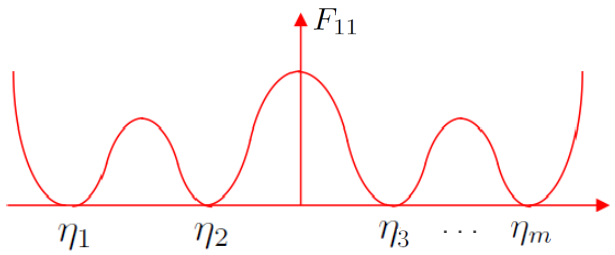

Fig. 8 Schematic of a multi-well energy landscape.

In complex moving interface problems such as fracture in ferroelectric ceramics, phase-field models are particularly interesting since a single partial differential equation governing the phase-field accomplishes at once (1) the tracking of the interfaces in a smeared way (cracks, domain walls) and (2) the modeling of the interfacial phenomena such as domain-wall energies or crack-face boundary conditions. Furthermore, the variational nature of these models makes the coupling of multiple physics very natural. Such a model has no difficulty in describing the nucleation of domains and cracks, and tracking the evolution of the domain boundaries and crack tips. This flexibility comes at the expense of a high computational cost, since the width of the phase-field regularizations of the domain wall and the crack must be resolved by the discretization for an accurate approximation of the sharp-interface model. Furthermore, the specific interface boundary or jump conditions under consideration must be encoded into the phase-field framework.

2.3 Phase-field model for ferroelectric single crystals

In the field of ferroelectric materials, given the extreme difficulty of tracking the interfaces (domain walls) explicitly with a sharp interface model, phase-field models are the current standard models for simulations of microstructure formation and evolution. According to these models, the Helmholtz free energy density of a ferroelectric material is stated as [110, 144]

$$\begin{aligned}\psi(\boldsymbol{\varepsilon},\mathbf{p},\nabla\mathbf{p},\mathbf{D}) = U(\nabla\mathbf{p}) + W(\mathbf{p},\boldsymbol{\varepsilon}) + \chi(\mathbf{p}) \\ + \tfrac{1}{2\varepsilon_0}(\mathbf{D}-\mathbf{p})\cdot(\mathbf{D}-\mathbf{p}),\end{aligned} \tag{2}$$

where $\mathbf{p}$ is the polarization, $\boldsymbol{\varepsilon}$ is the strain tensor associated with the mechanical displacement $\mathbf{u}$, $\boldsymbol{\varepsilon} = 1/2(\nabla\mathbf{u} + \nabla^T\mathbf{u})$, ε_0 is the permittivity of free space, and U is the domain wall energy density penalizing sharp variations in the polarization. The combination of energy functions χ and W is the total Landau-Devonshire energy density, penalizing deviations from the spontaneous polarizations and strains of the material, hence introducing the anisotropy and nonlinearity of ferroelectric materials. The first three terms in Eq. (2) indicate the free energy of the material and the last term is the free energy of the free space occupied by the material. The electric displacement $\mathbf{D}$ is defined as $\mathbf{D} = \varepsilon_0\mathbf{E} + \mathbf{p}$, $\mathbf{E}$ being the electric field associated with the electric potential ϕ, $\mathbf{E} = -\nabla\phi$. Following a Legendre transformation, the electromechanical enthalpy density $\mathcal{H}$ is obtained [110]

$$\begin{aligned}\mathcal{H}(\boldsymbol{\varepsilon},\mathbf{p},\nabla\mathbf{p},\mathbf{E}) &= \min_{\mathbf{D}}\left[\psi(\boldsymbol{\varepsilon},\mathbf{p},\nabla\mathbf{p},\mathbf{D}) - \mathbf{E}\cdot\mathbf{D}\right] \\ &= U(\nabla\mathbf{p}) + W(\mathbf{p},\boldsymbol{\varepsilon}) + \chi(\mathbf{p}) \\ &\quad - \frac{\varepsilon_0}{2}|\mathbf{E}|^2 - \mathbf{E}\cdot\mathbf{p}.\end{aligned} \tag{3}$$

The stresses and electric displacements are derived from the electrical enthalpy as $\boldsymbol{\sigma} = \partial\mathcal{H}/\partial\boldsymbol{\varepsilon}$ and $\mathbf{D} = -\partial\mathcal{H}/\partial\mathbf{E}$. The energy functions U, W and χ in Eq. (3) are chosen following [22, 23], adapted to a plane polarization and plane strain state:

$$U(p_{i,j}) = \frac{a_0}{2}(p_{1,1}^2 + p_{1,2}^2 + p_{2,1}^2 + p_{2,2}^2), \tag{4}$$

$$\begin{aligned}W(p_i,\varepsilon_{jk}) = &-\frac{b_1}{2}(\varepsilon_{11}p_1^2 + \varepsilon_{22}p_2^2) - \frac{b_2}{2}(\varepsilon_{11}p_2^2 + \varepsilon_{22}p_1^2) \\ &- b_3(\varepsilon_{21}+\varepsilon_{12})p_1p_2 + \frac{c_1}{2}(\varepsilon_{11}^2 + \varepsilon_{22}^2) \\ &+ c_2\varepsilon_{11}\varepsilon_{22} + \frac{c_3}{2}(\varepsilon_{12}^2 + \varepsilon_{21}^2),\end{aligned} \tag{5}$$

$$\begin{aligned}\chi(p_i) = &\alpha_1(p_1^2 + p_2^2) + \alpha_{11}(p_1^4 + p_2^4) + \alpha_{12}(p_1^2p_2^2) \\ &+ \alpha_{111}(p_1^6 + p_2^6) + \alpha_{112}(p_1^2p_2^4 + p_2^2p_1^4) \\ &+ \alpha_{1111}(p_1^8 + p_2^8) + \alpha_{1112}(p_1^6p_2^2 + p_2^6p_1^2) \\ &+ \alpha_{1122}(p_1^4p_2^4),\end{aligned} \tag{6}$$

where a_0 is the scaling parameter of the domain wall energy, $b_i (i = 1,2,3)$ are the constants of the coupling terms between strain and polarization and $c_i (i = 1,2,3)$ are the elastic constants. The coupling constants $b_i (i = 1,2,3)$ are obtained by fitting the spontaneous strains of

the tetragonal phase relative to the parent cubic phase. The eighth-order terms with coefficients α_{1111}, α_{1112}, and α_{1122} reproduce the dielectric behavior of barium titanate ($BaTiO_3$) single crystals [68, 127]. The eighth-order term with coefficient α_{1122} also retains a reasonable energy barrier for 90^0 domain switching in the tetragonal phase [144]. α_1 is linearly dependent on temperature and its negative value makes the cubic phase unstable. α_{11}, α_{12} and α_{1111} are evaluated from linear and nonlinear dielectric measurements above the Curie temperature. α_{111} is estimated by fitting the spontaneous polarization of the tetragonal phase. α_{112} and α_{1112} are fitted to the dielectric permittivity perpendicular to the spontaneous polarization [68, 127]. The constants are chosen to fit the behavior of single crystals of $BaTiO_3$ at room temperature, with a spontaneous polarization of p_0=0.26 C/m^2, and the relative spontaneous strains ε_a = -0.44% along a-axis and ε_c = 0.65% along c-axis [127, 144]. With these parameters, the normalized Landau-Devonshire energy is presented in Fig. 9 as a function of the normalized polarization p_1' and p_2', for a stress-free state ($\sigma_{ij} = 0$). The four minima in Fig. 9 correspond to the four variants of the tetragonal phase with normalized polarization p' = (1,0),(0,1),(-1,0) and (0,-1). The dimensionless variables are selected through the following normalizations: $x_i' = x_i\sqrt{c_0/a_0}/p_0$, $p_i' = p_i/p_0$, $\varepsilon_0' = \varepsilon_0 c_0/p_0^2$, $\phi' = \phi/\sqrt{a_0 c_0}$, $\alpha_1' = \alpha_1 p_0^2/c_0$, $\alpha_{11}' = \alpha_{11}p_0^4/c_0$, $\alpha_{12}' = \alpha_{12}p_0^4/c_0$, $\alpha_{111}' = \alpha_{111}p_0^6/c_0$, $\alpha_{112}' = \alpha_{112}p_0^6/c_0$, $\alpha_{1111}' = \alpha_{1111}p_0^8/c_0$, $\alpha_{1112}' = \alpha_{1112}p_0^8/c_0$, $\alpha_{1122}' = \alpha_{1122}p_0^8/c_0$, $b_i' = b_i p_0^2/c_0$ and $c_i' = c_i/c_0$, where i = 1,2,3, and c_0 = 1 GPa. The domain wall scaling parameter is set to $a_0 = 3.7 \times 10^{-9}\mathrm{Vm^3C^{-1}}$, which leads to the value of 0.5 nanometer for the normalized unit length $\Delta x' = 1$. The normalized parameters are presented in Table 1.

2.4 Phase-field model for brittle fracture

The variational regularized formulation of Griffith's fracture theory was first proposed in [28]. This model admits a straightforward numerical implementation [9, 15, 16, 17] and allows naturally for crack nucleation, branching, and interaction between multiple cracks. This approach smears the cracks which are not boundaries of the computational domain but rather features of the solution within the domain. This in contrast with sharp crack models such as cohesive methods [18, 134], the extended finite element method (XFEM) [84] and the strong discontinuity approach [85], which require the crack surfaces to be tracked algorithmically. If the mesh is sufficiently fine, the method used here is mesh independent, and it avoids difficulties of XFEM approaches to fracture, notably nucleation and branching.

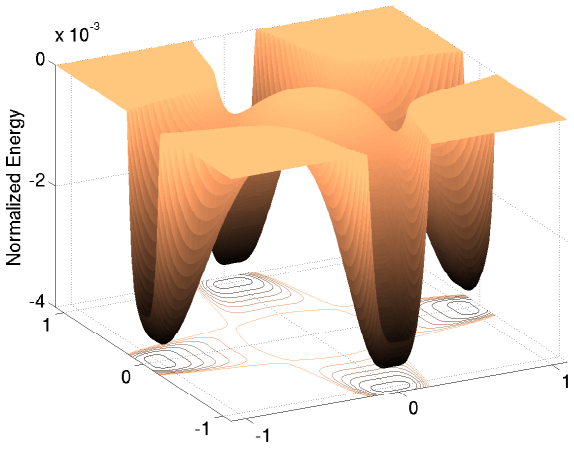

Fig. 9 Multi-well Landau-Devonshire energy density as a function of the normalized polarization components p_1' and p_2' in a stress-free state. Positive values are truncated to zero for clarity. The four minima correspond to the four variants of the tetragonal phase.

Following [16], the total energy of a body made of brittle material and occupying a region Ω is written as:

$$E_\kappa[\mathbf{u}, v] = \int_\Omega (v^2 + \eta_\kappa) F(\boldsymbol{\varepsilon}(\mathbf{u}))\, \mathrm{d}\Omega + G_c \int_\Omega \left[\frac{(1-v)^2}{4\kappa} + \kappa |\nabla v|^2 \right] \mathrm{d}\Omega - \int_{\Gamma_{N,\mathbf{u}}} \mathbf{t}\cdot\mathbf{u}\, \mathrm{d}S, \tag{7}$$

where F is the elastic potential as a function of the strain $\boldsymbol{\varepsilon}$, and G_c is the critical energy release rate or the surface energy density in Griffith's theory [36]. The elastic potential F is the stored energy density as a result of deformation of an elastic body. For a linear elastic material, this potential is a quadratic function of the strain, i.e. $F(\boldsymbol{\varepsilon}(\mathbf{u})) = \frac{1}{2}\boldsymbol{\varepsilon}(\mathbf{u})\colon \mathbf{C}\colon \boldsymbol{\varepsilon}(\mathbf{u})$, where $\mathbf{C}$ is the elastic stiffness tensor. The scalar phase field v describes a smooth transition in space between unbroken ($v = 1$) and broken ($v = 0$) states of the material. κ is a positive regularization constant to regulate the size of the fracture zone and η_κ is a small (relative to κ) residual stiffness to avoid the singularity of the first part of the energy in fully fractured regions of the domain. This functional is minimized in subsequent load increments, developing localized regions with low or zero values of v, where the smeared crack is located. During the incremental process, an irreversibility condition is also imposed, namely that the field v can only decrease at any point in space.

It has been shown that when the regularization parameter κ tends to zero, this regularized theory converges to the sharp theory of brittle fracture [17] and the

Table 1 Normalized parameters

c'_1	c'_2	c'_3	b'_1	b'_2	b'_3	α'_1	α'_{11}
185	111	74	1.4282	-0.185	0.8066	-0.0023	-0.0029
α'_{12}	α'_{111}	α'_{112}	α'_{1111}	α'_{1112}	α'_{1122}	ε'_0	
-0.0011	0.003	-0.00068	0.001	0.0093	1.24	0.131	

traction-free conditions on the crack faces of the sharp model are recovered. For a finite but small value of the regularization parameter, as used in practical computations, the resulting solutions are very close to being traction-free in the smeared crack. For ferroelectric materials, similar conditions can also be considered for the electrical fields, as discussed in Sections 3 and 4.

The crack propagates due to the competition between the first and second energy terms in Eq. (7). These terms can be interpreted as the bulk stored elastic energy and the surface energy, respectively. In a given region, the elastic energy density F increases due to the application of load. To release this energy for propagating the crack, the system decreases the value of v towards zero in that region. On the other hand, decreasing the value of v leads to an increase in the surface energy since deviations from 1 are penalized. Furthermore, variations of v are also penalized in the surface energy, resulting in the formation of smeared cracks whose width is governed by the regularization parameter κ. The surface energy increases proportionally by increasing the value of the critical energy release rate G_c of the material. Consequently, a higher value of the elastic energy is required to nucleate or propagate cracks. When κ tends to zero, the integrand of the surface energy term converges to the surface area of the crack, as expected in the sharp interface model. It was shown in practical computations with linear triangular elements that the surface energy is overestimated by a factor $1 + h/4\kappa$, where h is the element size [9, 17].

Figure 10 presents an illustration of the diffuse crack which is obtained from a minimizer of the energy in two dimensions with respect to v. The minimization leads to an optimal profile as a function of a point x on the crack, stated as [17]

$$v_\kappa(x) := \begin{cases} 0 & \text{if } d(x) \le \alpha \\ 1 - \exp(-\frac{d(x)-\alpha}{2\kappa}) & \text{otherwise,} \end{cases} \tag{8}$$

where $d(x)$ is a distance function considering a line orthogonal to the crack and 2α indicates the fully fractured region where $v = 0$. The semicircular area in front of the crack is obtained by considering a distance function of $d(r)$ along the radius of the circle r. The resulting contour in Fig. 10 introduces a pre-crack as an internal layer in a test specimen and initializes the scalar field v. This is in contrast to the sharp-crack models, where the crack faces are geometrically defined in the computational model.

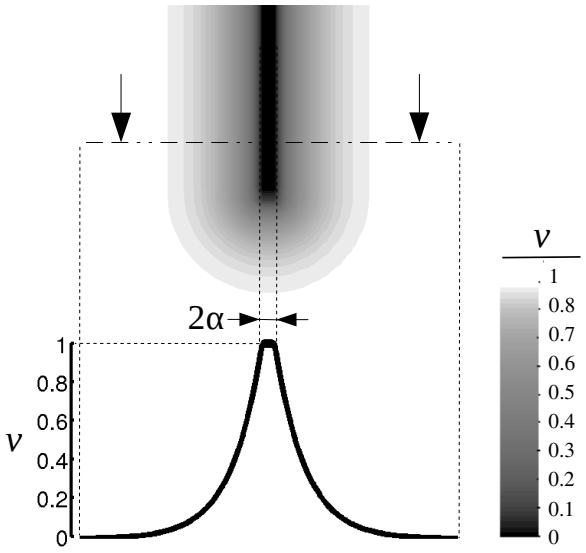

Fig. 10 A sample of the smeared crack using the profile in Eq. (8).

Considering a fixed v or $\mathbf{u}$, the total energy in Eq. (7) is quadratic and convex and the minimizer of either $E_\kappa(\mathbf{u}, \bullet)$ or $E_\kappa(\bullet, v)$ exists and is unique. An iterative algorithm of these two minimizers in subsequent load increments leads to a straightforward numerical implementation of this approach. The iterations continue until the field v reaches a steady state for each load increment. To avoid crack healing, the irreversibility condition is also imposed in this algorithm by fixing the field v to 0 when and where it reaches a given small threshold [15, 17].

3 Coupled phase-field model of fracture in ferroelectric single crystals

3.1 Phase-field models

To study the quasi-static crack propagation in ferroelectric materials, we have proposed a phase-field model [1], coupling two energetic phase-field approaches for ferroelectric domain formation and evolution and brittle

fracture, summarized in Sections 2.3 and 2.4, respectively. The coupling is done by forming a total electromechanical enthalpy that includes the enthalpy of a possibly fractured ferroelectric material, together with the fracture surface energy. The coupling between the field v representing the crack and the other fields depends on the particular electrical and mechanical boundary conditions adopted for the crack. Since the crack faces are represented by an internal layer in the phase-field model, these boundary conditions become part of the field equations. By way of example, mechanically traction-free condition is commonly assumed for the crack faces, i.e. $\boldsymbol{\sigma} \cdot \mathbf{n} = 0$ on the crack faces, $\mathbf{n}$ being the unit outward normal. Multiplying the jump set function $(v^2 + \eta_\kappa)$ by the electro-elastic energy density W in Eq. (3) satisfies this condition since W involves the elastic strains in all its terms.

There are two classical extreme assumptions for the electrical boundary conditions of crack faces in electromechanical materials. The first one assumes that the crack faces are closed and the electric field is not perturbed by the presence of the crack [87]. This assumption is called permeable conditions. The second assumption is termed impermeable conditions which were proposed to define an open and electrically defective crack by assuming zero permittivity for the crack gap [21]. To encode the permeable conditions in the phase-field model, the last two terms in the electromechanical enthalpy density $\mathcal{H}$ in Eq. (3), which involve the electric field $\mathbf{E}$, should remain unmodified. In contrast, the impermeable crack does not sustain any electric displacement inside the fractured zone ($v = 0$) and thus the last two terms of the electromechanical enthalpy density $\mathcal{H}$ in Eq. (3) are multiplied by the jump set function $(v^2 + \eta_\kappa)$ accordingly. For both permeable and impermeable conditions, we also assume that the polarization distribution near each side of the crack is unaffected by it, and hence dictated by the bulk material model. These conditions are called free-polarization boundary conditions [119], implying that the gradients normal to the crack faces of the polarization components vanish at the crack faces. In the phase-field framework, we introduce these conditions by multiplying the only term in $\mathcal{H}$ involving the gradient of polarization, i.e. the domain wall energy density U, by the jump set function $(v^2 + \eta_\kappa)$.

In summary, for a *traction-free, electrically permeable*, and *free-polarization* crack, the electromechanical enthalpy density $\mathcal{H}$ takes the form [1]

$$\begin{aligned}\mathcal{H}(\boldsymbol{\varepsilon}, \mathbf{p}, \nabla\mathbf{p}, \mathbf{E}, v) =& (v^2 + \eta_\kappa)\left[U(\nabla\mathbf{p}) + W(\mathbf{p}, \boldsymbol{\varepsilon})\right] \\ &+ \chi(\mathbf{p}) - \frac{\varepsilon_0}{2}|\mathbf{E}|^2 - \mathbf{E}\cdot\mathbf{p},\end{aligned} \tag{9}$$

while for a *traction-free, electrically impermeable*, and *free-polarization* crack, the electromechanical enthalpy density $\mathcal{H}$ follows [1]

$$\begin{aligned}\mathcal{H}(\boldsymbol{\varepsilon}, \mathbf{p}, \nabla\mathbf{p}, \mathbf{E}, v) =& (v^2 + \eta_\kappa)\left[U(\nabla\mathbf{p}) + W(\mathbf{p}, \boldsymbol{\varepsilon})\right] \\ &+ \chi(\mathbf{p}) + (v^2 + \eta_\kappa)\left[-\frac{\varepsilon_0}{2}|\mathbf{E}|^2 - \mathbf{E}\cdot\mathbf{p}\right],\end{aligned} \tag{10}$$

We illustrate in Section 4 that indeed these methods produce numerical solutions satisfying the assumed boundary conditions at the crack faces in an approximate but accurate way for a small value of the regularization parameter. The mathematical description of different crack-face boundary conditions is also presented in Section 4.

Given the electromechanical enthalpy density $\mathcal{H}$ for both crack models in Eqs. (9) and (10), the total electromechanical enthalpy for a ferroelectric body occupying a region Ω is written as

$$\begin{aligned}H[\mathbf{u}, v, \mathbf{p}, \phi] =& \int_\Omega \mathcal{H}(\boldsymbol{\varepsilon}(\mathbf{u}), \mathbf{p}, \nabla\mathbf{p}, \mathbf{E}(\phi), v)\ \mathrm{d}\Omega \\ &+ G_c \int_\Omega \left[\frac{(1-v)^2}{4\kappa} + \kappa|\nabla v|^2\right]\ \mathrm{d}\Omega \\ &- \int_{\Gamma_{N,\mathbf{u}}} \mathbf{t}\cdot\mathbf{u}\ \mathrm{d}S + \int_{\Gamma_{N,\phi}} \omega\phi\ \mathrm{d}S.\end{aligned} \tag{11}$$

The form of the variations of the electromechanical enthalpy along with a simple algorithm to solve the coupled system are presented in [1].

3.2 Numerical simulations

3.2.1 Mechanical loading

To perform numerical simulations, a rectangular domain is considered and a monotonically increasing mechanical load is applied by pulling the top and bottom sides of the model with a uniform vertical mechanical displacement. The three snapshots of the evolution of the microstructure and the crack are presented in Fig. 11 for the permeable model. By increasing the load, the crack and ferroelectric domains propagate through the sample and the formation of multiple twins is obvious in Fig. 11(a). To evaluate the effect of twinning on the crack propagation, the evolution of the total surface energy is presented in Fig. 12 as a function of the load step. Note that the surface energy is an indirect measure of the crack length. The graph is marked with letters **a** - **c** which correspond to three snapshots presented in Fig. 11. The surface energy graph is also obtained for a single-phase material by running the simulation with a frozen polarization field, which can be viewed as a

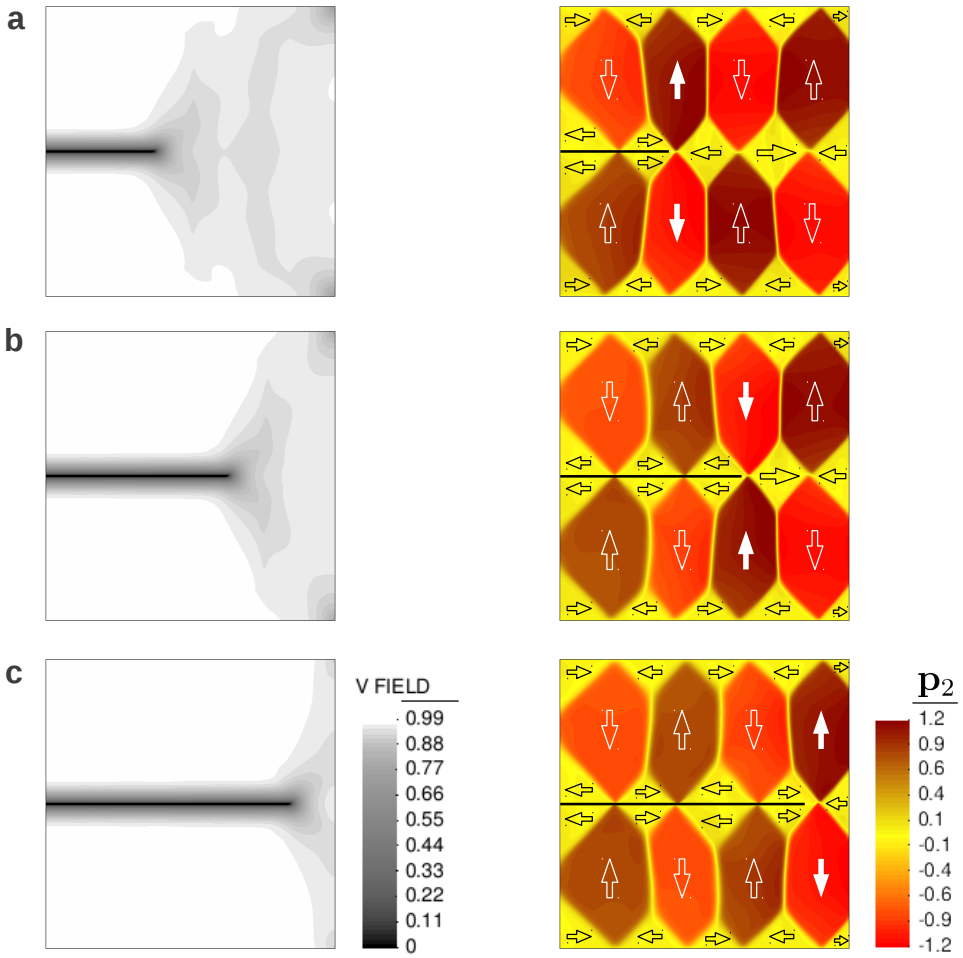

Fig. 11 Three snapshots of the evolution of the microstructure and the permeable crack. Domain structure is highlighted by the vertical polarization field $\mathbf{p}_2$ in the right column. The left column shows the field v representing the fractured area. The points where $v = 0$ are represented in black in the polarization maps to show the crack position.

reference to be compared with the multi-phase model and to assess the effect of twinning.

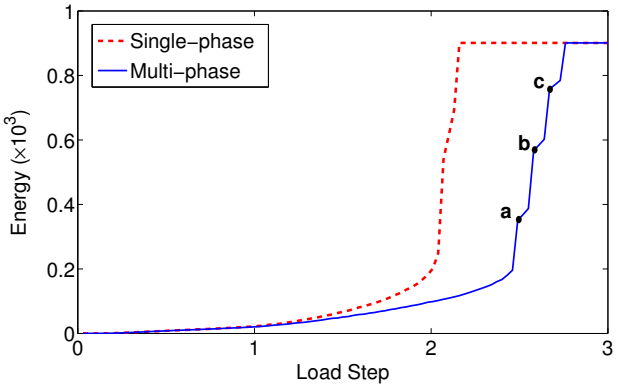

Fig. 12 Evolution of the normalized surface energy as a function of the load step.

The multi-phase model shows a slower growth rate than the single-phase one in Fig. 12. This deviation is attributed to the retarding effect on the crack propagation of the 90^o ferroelastic domain switching in the vicinity of the crack tip. This toughening mechanism is also reported in experiments of crack propagation in $BaTiO_3$ [80, 81]. Figure 12 also shows a sequence of abrupt crack propagation events, subsequent crack arrest, and slow crack propagation periods for the multi-phase model. The points **a** - **c** highlight the starting points of the slow propagation periods corresponding to the snapshots in Fig. 11(a)-(c). Each set of twins, highlighted by the bold white arrows in Fig. 11, induce compressive stresses ahead of the crack. Therefore, the crack propagates slowly until the loading is high enough to overcome the compressive stresses. As the crack cuts a set of twins, it can propagate easily until it feels the compressive stresses of the next set of twins. This process repeats itself until the complete

failure of the model. It is noteworthy that the experimental results in [27] show a similar slow-fast crack propagation behavior in a poled $BaTiO_3$ single crystal specimen under mechanical loading.

3.2.2 Electro-mechanical loading

Simulations are also performed under a combined electromechanical loading. The application of an electric field affects the size and position of the twins, as well as the polarization intensity. Consequently, the behavior of the system becomes more complex. Our simulation results show that, by applying a high electric field parallel or anti-parallel to the initial polarization, the coercive stress σ_c for 90^o ferroelastic domain switching increases and twinning becomes more difficult. A physical consequence is the shrinking of the twins, de-twinning, ahead of the crack. Figure 13 presents an illustration of the twins forming under the positive electric field $E = 3 \times 10^{-3}$ (parallel to the initial polarization). It is apparent from this figure that the horizontal domains (black arrows) align as much as possible with the applied electric field and are significantly larger than the vertical twins (white arrows). The shrinkage of the vertical twins is also obvious with respect to Fig. 11(c). Due to the de-twinning effect, the crack splits the model under a lower load and the effective fracture toughness decreases approaching the single-phase model. The application of higher electric fields leads to the total de-twinning of the model, and the surface energy graphs are almost identical to that of the single-phase.

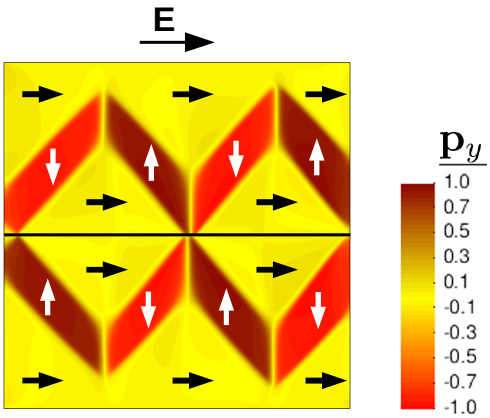

Fig. 13 Twinning under electromechanical loading. The electric field E with a normalized magnitude of 3×10^{-3} is applied parallel to the initial polarization. The black line shows the crack path and the bold black arrows indicate the domains aligned with the applied electric field.

4 Modeling of different crack-face boundary conditions

Crack-face boundary conditions have a strong effect on the fracture behavior of piezoelectrics and ferroelectrics, and ultimately on the reliability of the devices. We have introduced briefly two coupled phase-field models in Section 3 considering some of these conditions. In this section, we present a general framework in the context of phase-field models, encompassing all the usual crack-face boundary conditions proposed in the literature for electromechanical materials [5]. The phase-field model of brittle fracture introduced briefly in Section 2.4 is viewed as a regularization of Griffith's sharp-crack model. Here, the main objective is to show that the regularized solutions converge to that of the corresponding sharp-crack model considering the different crack-face boundary conditions. Again, note that here the cracks are not boundaries of the computational domain, and hence the different sharp-crack conditions have to be encoded into the phase-field framework.

4.1 Phase-field models

In the context of sharp-crack models in electromechanical materials, the most common crack-face boundary conditions in the literature can be classified as follows [5]:

A. Uncoupled electrical/mechanical crack-face conditions
   Mechanical boundary conditions: These are mainly: (1) traction-free crack faces and (2) cohesive zone models [18, 134] introducing a traction-separation law on the crack faces. Here, we consider only traction-free crack boundary conditions. The encoding of the cohesive crack-face conditions is the subject of a future work.
   Electrical boundary conditions: These are mainly (1) permeable, (2) impermeable and (2) semi-permeable crack models, each assuming different electrical properties of the crack gap [66]. The permeable and impermeable conditions are introduced in Section 3. However, both conditions neglect the effect of the medium filling the crack gap and they are not physically justifiable in many cases. As an improvement, semi-permeable boundary conditions were introduced to treat the crack gap as a linear dielectric material with a finite permittivity [42]. A physical inconsistency of the semi-permeable conditions is that the stored electric charge in the crack gap induces a closing traction on the crack faces which is not considered in these conditions.

B. Coupled electromechanical crack-face conditions.
To overcome the inconsistency of the semi-permeable boundary conditions, the Energetically Consistent (EC) crack model was first proposed by considering not only the electric charge inside the crack gap, but also the corresponding induced closing traction on the crack faces [62]. In this model, the crack acts as a capacitor inside the material. EC conditions are more physically realistic than the other conditions.

C. Polarization boundary conditions.
Modeling of cracks in ferroelectric materials requires the imposition of some conditions for the polarization distribution on the crack faces [123]. Free- and zero-polarization conditions are two usual choices. The former is a homogeneous Neumann boundary condition for the polarization dictated by the bulk material model. The latter is a homogeneous Dirichlet boundary condition for the polarization, thereby modeling an open crack filled with free space.

Table 2 summarizes different crack-face boundary conditions as described above along with related mathematical descriptions.

In the following, we first focus on the phase-field formulation of these conditions for fracture in piezoelectrics based on the linear theory of piezoelectricity where microstructure effects are not taken into account. Due to their simplicity, these models are useful to study the basic concepts of the linear theory in the context of fracture mechanics and to evaluate the effects of individual and coupled electromechanical fields.

According to the linear theory of piezoelectricity, the electromechanical enthalpy density $\mathcal{H}$ of a piezoelectric material is stated as [115]

$$\mathcal{H}(\boldsymbol{\varepsilon},\mathbf{E}) = \frac{1}{2}(\boldsymbol{\varepsilon}-\boldsymbol{\varepsilon}^r):\mathbb{C}:(\boldsymbol{\varepsilon}-\boldsymbol{\varepsilon}^r) - (\boldsymbol{\varepsilon}-\boldsymbol{\varepsilon}^r):\mathbf{e}^T\cdot\mathbf{E} - \mathbf{p}^r\cdot\mathbf{E} - \frac{1}{2}\mathbf{E}\cdot\mathbf{K}\mathbf{E}, \tag{12}$$

where $\mathbf{e}$ is the tensor of piezoelectric coupling constants, $\boldsymbol{\varepsilon}^r$ is the remanent strain, $\mathbf{p}^r$ is the remanent polarization, and $\mathbf{K}$ is the dielectric tensor. In order to encode different crack-face boundary conditions, different terms of the electromechanical enthalpy density in Eq. (12) are multiplied by the jump set function $(v^2+\eta_\kappa)$. For traction-free and impermeable conditions, the jump set should be multiplied by the energy terms associated with the strain $\boldsymbol{\varepsilon}$ and the electric field $\mathbf{E}$, respectively. In contrast, the permeable conditions imply that the energy terms associated with the electric field $\mathbf{E}$ remain unmodified by the jump set. EC conditions assume that the crack behaves electrically similar to a capacitor, storing electrical charge between the capacitor plates. Here, we develop a general formulation of this enthalpy in the context of the phase-field model. The proposed enthalpy is stated as [5]

$$H_c = -\frac{\varepsilon_0}{2}\int_\Omega \left(1-v^2\right)|\mathbf{F}^{-T}\nabla\phi|^2 J\,\mathrm{d}\Omega, \tag{13}$$

where $\mathbf{F}$ is the deformation gradient tensor defined as $\mathbf{F}=\mathbf{I}+\nabla\mathbf{u}$, $\mathbf{I}$ is the identity matrix and J is the Jacobian of the deformation defined as $J=\det\mathbf{F}$. The jump set function $\left(1-v^2\right)$ restricts the added enthalpy to the fracture zone. The electric field in the deformed configuration of the fracture zone is $\mathbf{E}_c=-\mathbf{F}^{-T}\nabla\phi$ and the enthalpy density is integrated over the area of the deformed body using the Jacobian of the deformation J. Then, the electromechanical enthalpy density of the EC crack model is obtained by adding the proposed electromechanical enthalpy of the diffuse crack in Eq. (13) to the enthalpy of the impermeable crack model. Table 3 summarizes the electromechanical enthalpy density, stresses and electric displacements for different crack-face boundary conditions in piezoelectric materials. Note that we take the remanent state of the material as the reference configuration, therefore the remanent strain ε^r and the remanent polarization $\mathbf{p}^r$ are set to zero.

Additional polarization boundary conditions should also be considered for ferroelectric materials since the polarization is not fixed and can be altered in a nonlinear fashion. To encode the zero- and free-polarization conditions, the energy terms in Eq. (3) associated with polarization $\mathbf{p}$ and the gradient of polarization $\nabla\mathbf{p}$ should be multiplied by the jump set function $(v^2+\eta_\kappa)$, respectively. Table 4 summarizes the electromechanical enthalpy density, stresses and electric displacements for different crack-face boundary conditions in ferroelectric materials. See [5] for a detailed discussion on different crack-face boundary conditions, corresponding governing equations and a general solution algorithm for the fracture models of piezoelectric and ferroelectric materials.

4.2 Verification

We perform numerical simulations aimed at verifying different aspects of the proposed models. We study the convergence of the energy-release rate as computed with the phase-field models summarized in Table 3 for piezoelectrics. In all cases stationary cracks are considered for simplicity. Figure 14 presents the energy-release rates

Table 2 Crack-face boundary conditions in electromechanical materials [5].

Crack-face boundary conditions			Mathematical description
Uncoupled	Mechanical	Traction-free	$\boldsymbol{\sigma}^+ \cdot \mathbf{n} = \boldsymbol{\sigma}^- \cdot \mathbf{n} = \mathbf{0}$
		Cohesive zone	$\boldsymbol{\sigma}^+ \cdot \mathbf{n} = \boldsymbol{\sigma}^- \cdot \mathbf{n} = \mathbf{t}$
	Electrical	Permeable	$\phi^+ = \phi^-$ $\mathbf{D}^+ \cdot \mathbf{n} = \mathbf{D}^- \cdot \mathbf{n}$
		Impermeable	$\mathbf{D}^+ \cdot \mathbf{n} = \mathbf{D}^- \cdot \mathbf{n} = 0$
Coupled	Electro-mechanical	Energetically Consistent (EC)	$\mathbf{D}^+ \cdot \mathbf{n} = \mathbf{D}^- \cdot \mathbf{n} = D_c = \varepsilon_0 E_c$ $\sigma_c = \varepsilon_0 E_c^2/2$ $\mathcal{H}_c = -\varepsilon_0 E_c^2/2$
Polarization	Free-polarization		$\nabla \mathbf{p}^+ \cdot \mathbf{n} = \nabla \mathbf{p}^- \cdot \mathbf{n} = \mathbf{0}$
	Zero-polarization		$\mathbf{p}^+ = \mathbf{p}^- = \mathbf{0}$

$\mathbf{p}$: Polarization, $\boldsymbol{\sigma}$: Stress, $\mathbf{D}$: Electric displacement, ϕ: Electric potential
$\mathbf{t}$: Mechanical traction governed by a traction-separation law
$\mathbf{n}$: Unit normal to top (+) and bottom (-) crack faces
E_c and D_c : Electric field and electric displacement induced in the crack gap
$\mathcal{H}_c$: Electrical enthalpy density of the crack gap

Table 3 Electro-mechanical enthalpy density, stresses and electric displacements for piezoelectric materials with different electromechanical crack conditions [5].

	Electro-mechanical enthalpy density	Stresses and Electric displacements
Per	$\mathcal{H} = (v^2 + \eta_\kappa)(\frac{1}{2}\boldsymbol{\varepsilon} : \mathbb{C} : \boldsymbol{\varepsilon} - \boldsymbol{\varepsilon} : \mathbf{e}^T \cdot \mathbf{E}) - \frac{1}{2}\mathbf{E} \cdot \mathbf{K}\mathbf{E}$	$\boldsymbol{\sigma} = (v^2 + \eta_\kappa)(\mathbb{C} : \boldsymbol{\varepsilon} - \mathbf{e}^T \cdot \mathbf{E})$ $\mathbf{D} = (v^2 + \eta_\kappa)\mathbf{e} : \boldsymbol{\varepsilon} + \mathbf{K}\mathbf{E}$
Imp	$\mathcal{H} = (v^2 + \eta_\kappa)(\frac{1}{2}\boldsymbol{\varepsilon} : \mathbb{C} : \boldsymbol{\varepsilon} - \boldsymbol{\varepsilon} : \mathbf{e}^T \cdot \mathbf{E}) - (v^2 + \eta_\kappa)(\frac{1}{2}\mathbf{E} \cdot \mathbf{K}\mathbf{E})$	$\boldsymbol{\sigma} = (v^2 + \eta_\kappa)(\mathbb{C} : \boldsymbol{\varepsilon} - \mathbf{e}^T \cdot \mathbf{E})$ $\mathbf{D} = (v^2 + \eta_\kappa)(\mathbf{e} : \boldsymbol{\varepsilon} + \mathbf{K}\mathbf{E})$
EC	$\mathcal{H} = (v^2 + \eta_\kappa)(\frac{1}{2}\boldsymbol{\varepsilon} : \mathbb{C} : \boldsymbol{\varepsilon} - \boldsymbol{\varepsilon} : \mathbf{e}^T \cdot \mathbf{E}) - (v^2 + \eta_\kappa)(\frac{1}{2}\mathbf{E} \cdot \mathbf{K}\mathbf{E}) - \frac{\varepsilon_0}{2}\left(1 - v^2\right)\left\|\mathbf{F}^{-T}\mathbf{E}\right\|^2 J$	$\boldsymbol{\sigma} = (v^2 + \eta_\kappa)(\mathbb{C} : \boldsymbol{\varepsilon} - \mathbf{e}^T \cdot \mathbf{E}) + \frac{J}{2}\left(1 - v^2\right)\boldsymbol{\sigma}_c$ $\mathbf{D} = (v^2 + \eta_\kappa)(\mathbf{e} : \boldsymbol{\varepsilon} + \mathbf{K}\mathbf{E}) + J\left(1 - v^2\right)\mathbf{F}^{-1}\mathbf{D}_c$

Per: Permeable (traction-free), Imp: Impermeable (traction-free)
EC: Energetically Consistent

$$\mathbf{D}_c = \varepsilon_0 \mathbf{E}_c = \varepsilon_0 \mathbf{F}^{-T}\mathbf{E},$$
$$\boldsymbol{\sigma}_c = \mathbf{F}^{-1}\left(\mathbf{D}_c \otimes \mathbf{E}_c\right) + \left(\mathbf{D}_c \otimes \mathbf{E}_c\right)\mathbf{F}^{-T} - \frac{\varepsilon_0}{2}|\mathbf{E}_c|^2\left(\mathbf{F}^{-1} + \mathbf{F}^{-T}\right)$$

in a four-point bending setup using two mesh sizes. Different electrical loads are applied perpendicular to the crack. In the case of the permeable crack, the applied electric field affects the computed energy release rate for the coarse mesh. This situation is readily corrected by refining the mesh and thereby reducing the regularization parameter κ. Indeed, for the resolved (fine) mesh it is interesting to observe that the value of energy release rate is insensitive to the magnitude of the applied electric field, in agreement with the results of the sharp-crack model obtained in [66]. In contrast, the impermeable conditions indicate a significant decrease of the energy release rate in the presence of applied electric fields. This behavior is interpreted as a strong retarding effect on the crack propagation. The behavior of the EC model is very close to that of the impermeable model for the coarse mesh, while showing a less significant retarding effect for the fine mesh. The con-

Table 4 Electro-mechanical enthalpy density, stresses and electric displacements for ferroelectric materials with different electromechanical crack conditions [5].

	Electro-mechanical enthalpy density	Stresses and Electric displacements
	Free-polarization	
Per	$\mathcal{H} = (v^2+\eta_\kappa)(U+W)+\chi$ $-\frac{\varepsilon_0}{2}\lvert\mathbf{E}\rvert^2 - \mathbf{E}\cdot\mathbf{p}$	$\boldsymbol{\sigma} = (v^2+\eta_\kappa)\frac{\partial W}{\partial \boldsymbol{\varepsilon}}$ $\mathbf{D} = \varepsilon_0\mathbf{E}+\mathbf{p}$
Imp	$\mathcal{H} = (v^2+\eta_\kappa)(U+W)+\chi$ $-(v^2+\eta_\kappa)(\frac{\varepsilon_0}{2}\lvert\mathbf{E}\rvert^2+\mathbf{E}\cdot\mathbf{p})$	$\boldsymbol{\sigma} = (v^2+\eta_\kappa)\frac{\partial W}{\partial \boldsymbol{\varepsilon}}$ $\mathbf{D} = (v^2+\eta_\kappa)(\varepsilon_0\mathbf{E}+\mathbf{p})$
EC	$\mathcal{H} = (v^2+\eta_\kappa)(U+W)+\chi$ $-(v^2+\eta_\kappa)(\frac{\varepsilon_0}{2}\lvert\mathbf{E}\rvert^2+\mathbf{E}\cdot\mathbf{p})$ $-\frac{\varepsilon_0}{2}\left(1-v^2\right)\lvert\mathbf{F}^{-T}\mathbf{E}\rvert^2 J$	$\boldsymbol{\sigma} = (v^2+\eta_\kappa)\frac{\partial W}{\partial \boldsymbol{\varepsilon}}$ $+\frac{J}{2}\left(1-v^2\right)\boldsymbol{\sigma}_c$ $\mathbf{D} = (v^2+\eta_\kappa)(\varepsilon_0\mathbf{E}+\mathbf{p})$ $+J\left(1-v^2\right)\mathbf{F}^{-1}\mathbf{D}_c$
	Zero-polarization	
Per	$\mathcal{H} = U+(v^2+\eta_\kappa)(W+\chi-\mathbf{E}\cdot\mathbf{p})$ $-\frac{\varepsilon_0}{2}\lvert\mathbf{E}\rvert^2-(1-v^2)\frac{\varepsilon_r-\varepsilon_0}{2}\lvert\mathbf{E}\rvert^2$	$\boldsymbol{\sigma} = (v^2+\eta_\kappa)\frac{\partial W}{\partial \boldsymbol{\varepsilon}}$ $\mathbf{D} = \varepsilon_0\mathbf{E}+(v^2+\eta_\kappa)\mathbf{p}$ $+(1-v^2)(\varepsilon_r-\varepsilon_0)\mathbf{E}$
Imp	$\mathcal{H} = U+(v^2+\eta_\kappa)(W+\chi)$ $-(v^2+\eta_\kappa)(\frac{\varepsilon_0}{2}\lvert\mathbf{E}\rvert^2+\mathbf{E}\cdot\mathbf{p})$	$\boldsymbol{\sigma} = (v^2+\eta_\kappa)\frac{\partial W}{\partial \boldsymbol{\varepsilon}}$ $\mathbf{D} = (v^2+\eta_\kappa)(\varepsilon_0\mathbf{E}+\mathbf{p})$
EC	$\mathcal{H} = U+(v^2+\eta_\kappa)(W+\chi)$ $-(v^2+\eta_\kappa)(\frac{\varepsilon_0}{2}\lvert\mathbf{E}\rvert^2+\mathbf{E}\cdot\mathbf{p})$ $-\frac{\varepsilon_0}{2}\left(1-v^2\right)\lvert\mathbf{F}^{-T}\mathbf{E}\rvert^2 J$	$\boldsymbol{\sigma} = (v^2+\eta_\kappa)\frac{\partial W}{\partial \boldsymbol{\varepsilon}}$ $+\frac{J}{2}\left(1-v^2\right)\boldsymbol{\sigma}_c$ $\mathbf{D} = (v^2+\eta_\kappa)(\varepsilon_0\mathbf{E}+\mathbf{p})$ $+J\left(1-v^2\right)\mathbf{F}^{-1}\mathbf{D}_c$

Per: Permeable (traction-free), Imp: Impermeable (traction-free), EC: Energetically Consistent

verged results of the phase-field models corresponding to the different crack-face conditions for the fine mesh, presented in Fig. 14, agree qualitatively with the results of the sharp-crack model obtained in [66].

We have also presented numerical evidence that the phase-field solutions satisfy the corresponding crack-face conditions in a diffuse sense and converge to the solutions of the corresponding sharp-crack model as the mesh size h and κ tend to zero in a concerted manner [5]. Figure 15 presents the results for the traction-free, impermeable crack model (see Table 3) along a cross section of the four-point bending sample normal to the crack and behind the crack tip. The cross-section of the diffuse cracks is presented by plotting the v field along the same section in Fig. 15(a). For comparison purposes, the same problem is solved with the corresponding sharp-crack model by geometrically introducing a pre-crack of the same length in the computational model. It is obvious in Fig. 15 that by decreasing the mesh size and the regularization parameter, the transition of the field v between the intact ($v = 1$) and fractured ($v = 0$) zones becomes sharper and the stresses and electric displacements recover the solutions of the sharp-crack model near the edges of the smeared crack.

We have performed analogous verification tests for the phase-field models of fracture in ferroelectrics summarized in Table 4. Similar conclusions have been obtained from the comparison of the stresses and electric displacements profiles across of the diffuse crack with

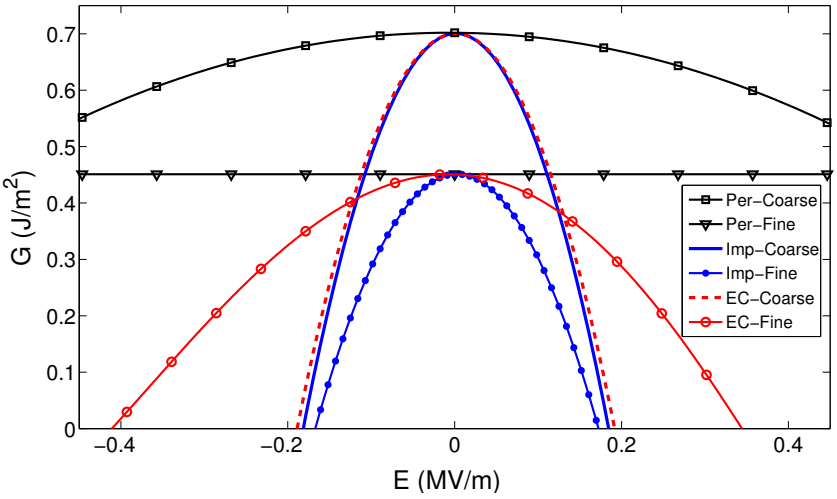

Fig. 14 Energy release rates for different crack face conditions: Permeable (Per), Impermeable (Imp) and air-filled Energetically Consistent (EC) as a function of applied electric field. The results are presented for coarse and fine meshes.

those computed for the sharp-crack. The polarization components also satisfy the free-polarization and zero-polarization conditions near the diffuse crack. As expected, since the crack-face boundary conditions are encoded for ferroelectrics by analogy to piezoelectrics, we are able to show that the phase-field solutions (1) satisfy the corresponding crack-face conditions in a diffuse manner and (2) converge to the corresponding sharp-crack solutions. Some of these results are presented in [1, 5].

4.3 Numerical simulations of propagating cracks

We have examined the effects of the different crack-face conditions on the crack propagation [5]. Figure 16 presents the crack growth as a function of the time in the piezoelectric four-point bending specimen. External electric fields $E = \pm 1$ MV/m are applied from time $t =$ 190 s. It is apparent that both the positive and negative electric fields arrest the impermeable crack while they do not affect the permeable crack growth rate. This rate for the EC conditions lies between that of the permeable and impermeable conditions. We also observe no sensitivity of the permeable and impermeable cracks to the sign of the applied electric field. In contrast, the air-filled EC crack shows an asymmetric response with respect to this sign. It is less retarded under the negative applied electric field than under the positive one. These observations, and in particular the asymmetric response of the EC crack model, are also apparent from the converged results of energy release rate in Fig. 14.

Similar simulations have also been carried out for ferroelectric materials and the effect of domain switching on the crack propagation is evaluated. The results are presented in Fig. 17 for the different crack-face conditions and under various applied electric fields. Similarly to piezoelectric materials, the strongest retarding effect on the crack propagation is observed for the impermeable conditions. It is also obvious that the crack growth increases with the application of the negative normalized electric field $E = -5 \times 10^{-3}$ for all the crack conditions. This weakening effect is more pronounced for the EC crack model. The normalized electric field $E = -10^{-2}$ (above the coercive field in magnitude) decreases the crack growth significantly and it shows a similar toughening effect to that of the positive applied electric fields.

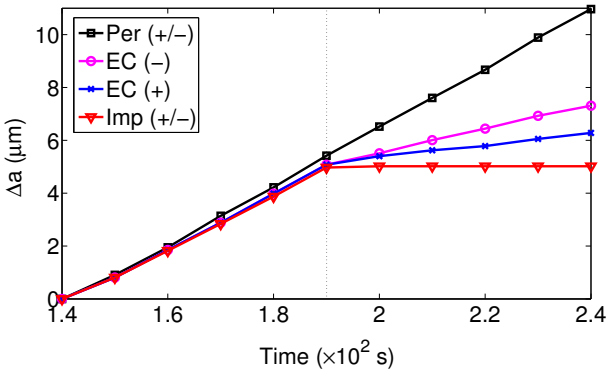

Fig. 16 Crack growth (Δa) as a function of the time in the piezoelectric material considering the Permeable (Per), Impermeable (Imp) and air-filled Energetically Consistent (EC) crack face conditions. External electric fields $E = \pm 1$ MV/m are applied from time $t = 190$ s. The + and - signs indicate a positive and negative applied electric field.

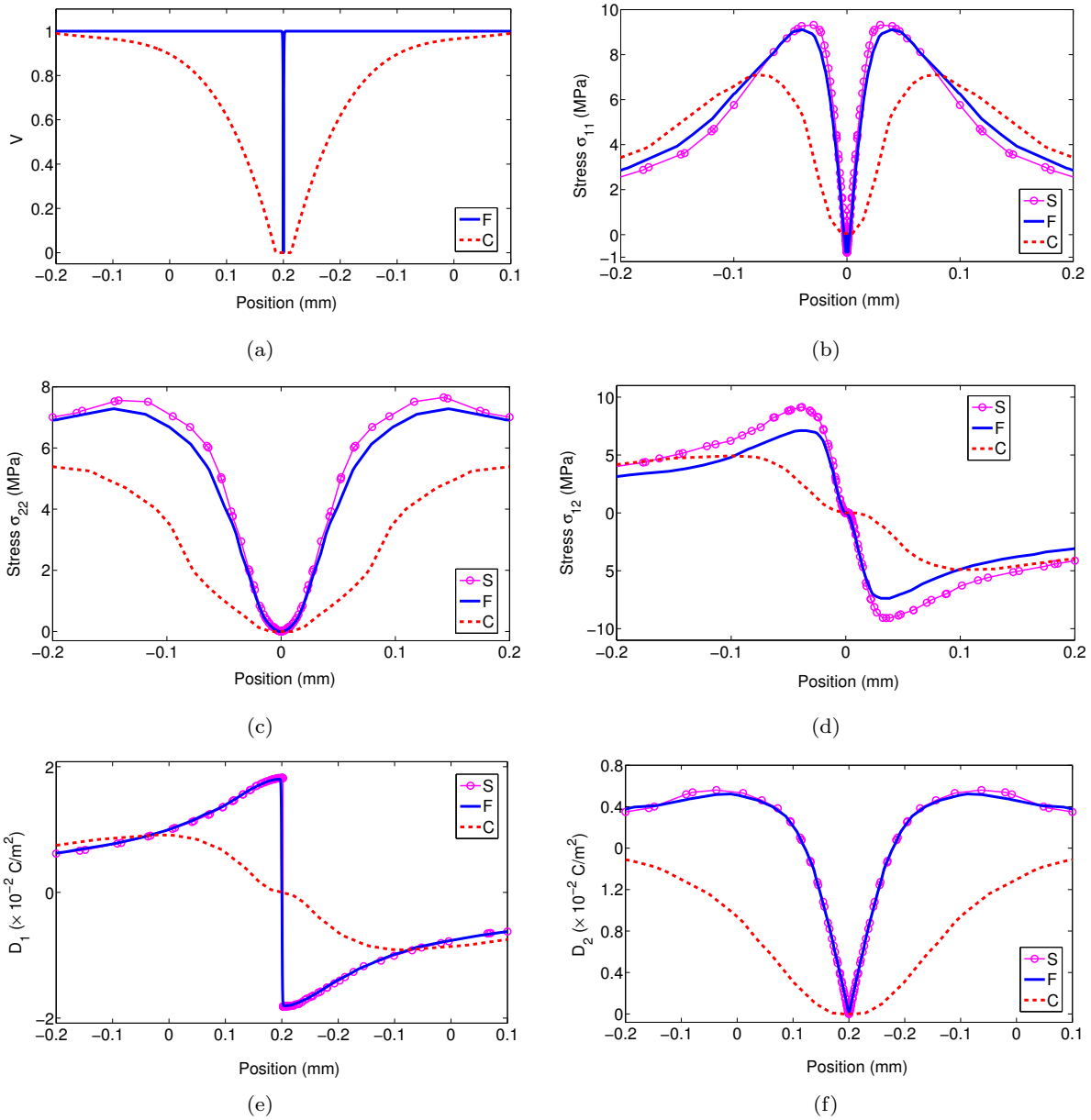

Fig. 15 (a) Field v along a cross section of the four-point bending sample normal to the crack and behind the crack tip, (b)-(f) Stresses and electric displacements along the same section. The results are obtained for a traction-free, electrically impermeable pre-crack. Different mesh sizes are chosen near the smeared crack for each simulation: F (fine mesh) and C (coarse mesh). A simulation is also done for the sharp-crack model (marked with S) with a fine mesh. The value of κ is chosen as four times of the smallest element size in each simulation.

5 Phase-field simulation of anisotropic crack propagation in ferroelectric single crystals

Formation and evolution of ferroelectric domains near the crack tip is responsible for changes in the fracture behavior of ferroelectric materials such as fracture toughness anisotropy. The Vickers indentation technique is commonly used in determining this anisotropy [75, 89, 101, 112, 116, 121]. These experimental observations show that the cracking along the poling direction of the material has a shorter length and consequently higher fracture toughness, and that normal to the poling direction has a longer length and lower fracture toughness. Ferroelastic domain switching is known as the main cause of the anisotropy. The main objective of this section is to introduce a model which can simulate the anisotropic crack growth under the Vickers indentation loading with the goal of linking the microstructural details with the macroscopic observable response [2]. For this purpose, the model proposed in Section 3

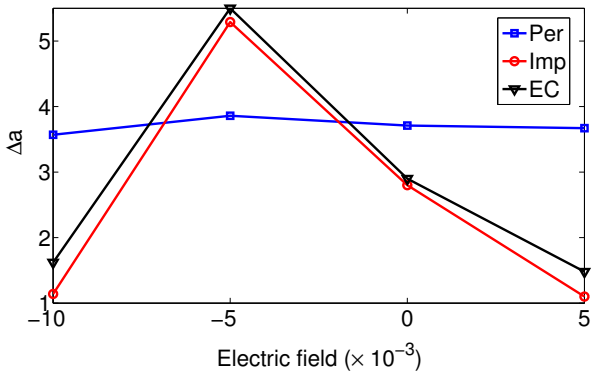

Fig. 17 Crack growth (Δa) as a function of the magnitude and sign of the electric field in the ferroelectric material. The results are obtained for the different crack face conditions: Permeable (Per), Impermeable (Imp) and air-filled Energetically Consistent (EC).

is modified following [9] by introducing a crack non-interpenetration condition in the variational approach to fracture accounting for the asymmetric behavior in tension and compression in the framework of linearized elasticity. Without this condition, the variational approach would lead to crack propagation and interpenetration near the indenter contact faces, where high compressive stresses are induced by the indentation loading.

We briefly describe here the coupled phase-field formulation with emphasis on the modification introduced to account for the asymmetric behavior in tension and compression. We form a total electromechanical enthalpy of a possibly fractured ferroelectric material occupying a region Ω as [2]

$$H[\mathbf{u},\mathbf{p},\phi,v] = \int_\Omega [W_e(\boldsymbol{\varepsilon}(\mathbf{u}),v) + W_f(\boldsymbol{\varepsilon}(\mathbf{u}),\mathbf{p},\phi,v)]\,\mathrm{d}\Omega + G_c\int_\Omega \left[\frac{(1-v)^2}{4\kappa} + \kappa|\nabla v|^2\right]\,\mathrm{d}\Omega, \quad (14)$$

where body loads, volume charges, tractions and surface charges have been ignored for simplicity. In the bulk energy (first integral), W_e is the part of the bulk energy density associated with the strain $\boldsymbol{\varepsilon}$ and W_f is the electromechanical energy density associated with the ferroelectric response. To account for the quite different fracture behavior in tension and compression, the energy density W_e is written in [9] as

$$W_e(\boldsymbol{\varepsilon},v) = \kappa_0\frac{\mathrm{tr}^-(\boldsymbol{\varepsilon})^2}{2} + (v^2+\eta_\kappa)\left(\kappa_0\frac{\mathrm{tr}^+(\boldsymbol{\varepsilon})^2}{2} + \mu\,\boldsymbol{\varepsilon}_D\cdot\boldsymbol{\varepsilon}_D\right), \quad (15)$$

where κ_0 and μ are the bulk and shear modulus of the material, respectively. The trace of the strain $\boldsymbol{\varepsilon}$ is decomposed in positive and negative parts, respectively as $\mathrm{tr}^+ = \max(\mathrm{tr}(\boldsymbol{\varepsilon}),0)$ and $\mathrm{tr}^- = \max(-\mathrm{tr}(\boldsymbol{\varepsilon}),0)$ and $\boldsymbol{\varepsilon}_D$ are the deviatoric components of the strain tensor. This decomposition is introduced to distinguish the contributions to the strain energy due to compression, expansion, and shear. In contrast to [1] and Section 3, here only the expansion and shear terms are multiplied by the jump set function $(v^2+\eta_\kappa)$ to prevent crack interpenetration in compressed regions.

The electromechanical energy density W_f associated with polarization $\mathbf{p}$, electric potential ϕ, $\boldsymbol{\varepsilon}$ and v is formulated as

$$W_f(\boldsymbol{\varepsilon},\mathbf{p},\phi,v) = (v^2+\eta_\kappa)[U(\nabla\mathbf{p}) + W_c(\mathbf{p},\boldsymbol{\varepsilon})] + \chi(\mathbf{p}) - \frac{\varepsilon_0}{2}|\nabla\phi|^2 + \nabla\phi\cdot\mathbf{p}, \quad (16)$$

where energy functions U and χ are defined in Eqs. (4) and (6), respectively and W_c equals the energy function W in Eq. (5) without the elastic energy terms (last three terms). This particular formulation of the phase-field model encodes the asymmetric fracture response in tension and compression, as well as the assumed crack conditions. Here, we assume the crack to be traction-free and electrically permeable. The governing equations and a solution algorithm are presented in detail in [2].

We consider an indentation impression lying inside a ferroelectric single crystal in two dimensions. A monotonically increasing mechanical load is applied by pulling the indentation faces with a uniform displacement. It is also assumed that the indenter faces are connected to the ground, therefore the electric potential is fixed to zero on the indentation faces. All the material parameters are selected to fit the behavior of single crystals of barium titanate ($BaTiO_3$), see Section 2.3. Figure 18 presents a snapshot of the crack propagation. The value of v starts to decrease towards zero around the vertices of the indentation as the load increases. After reaching the zero value, the fracture zone grows along the four radial directions as shown in Fig. 18.

The value of surface energy (the second integral in Eq. (14)) is calculated in each of the four equally large areas around the corners of the indentation in Fig. 18. The surface energy graphs are shown in Fig. 19. It is obvious that the surface energies of zones 1 and 3 are larger than those of zones 2 and 4, i.e. the perpendicular cracks to the polarization are longer than the parallel ones. This is a clear evidence of the anisotropic crack propagation in agreement with experimental observations.

Domain switching during crack growth is responsible for the observed fracture toughness anisotropy. Figure 20 presents a snapshot of the domain evolution in

an area around the indentation. The polarization vectors indicate wing-shaped domains or twins around the tip of the parallel cracks (cracks 2 and 4). This kind of switching is induced by high tensile stresses near the crack tip tending to elongate the material in the horizontal direction in front of the parallel cracks. The perpendicular cracks grow more than parallel ones due to the absence of ferroelastic domain switching. Therefore, the effective fracture toughness is lower perpendicular to the poling direction.

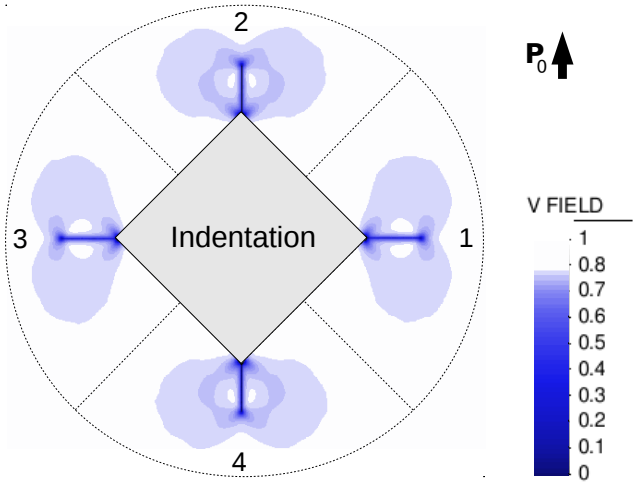

Fig. 18 Snapshot of the fracture evolution. Field v represents the fracture area. Four equally large areas around the corners of the indentation are considered to obtain the surface energy evolution of the four radial cracks (crack zones $1-4$) shown in Fig. 19.

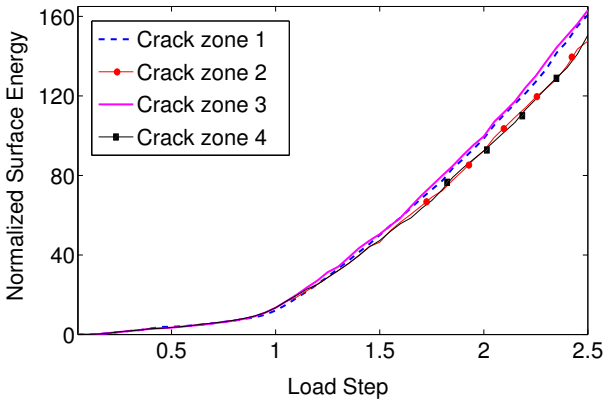

Fig. 19 Evolution of the normalized surface energy of the four zones (crack zones $1-4$) marked in Fig. 18 as a function of the load step.

6 Crack initiation patterns at electrode edges in multilayer ferroelectric actuators

Multilayer ferroelectric actuators have been widely used in various applications, including microprecision cutting machines, inkjet printer heads, laser printers, optical disk drives and laser tuning [91, 118], to mention a few. Internal electrodes are commonly employed in the structures of multilayer actuators. Experiments reported that electrode edges are the main source of fracture in these actuators [8, 31, 56, 71, 72, 117, 146]. This is due to the generation of non-uniform electric fields in the vicinity of electrode edges, which in turn induce incompatible strain fields and hence concentrated stresses. Numerous investigations have been carried out during the past decades to understand the fracture behavior of multilayer actuators. Theoretical models have been developed for fracture mechanics analysis of multilayer ceramics based on the electrostrictive theory [34, 43, 99, 131, 137], the linear theory of piezoelectricity [38, 67, 98, 126, 139], and nonlinear approaches taking into account the ferroelectric and ferroelastic behaviors [24, 53, 72, 146]. Using these models, the electromechanical fields can be analyzed near the electrode edge and some design criteria regarding the geometry of the actuators and electrodes can be proposed to reduce the probability of fracture from the electrode edge. However, the crack propagation mechanisms of the actuators have not been studied in these models and these mechanisms are still unclear due to the complex interactions between the propagating cracks, electromechanical fields and microstructure of the material near the electrode edge. The potential of the phase-field approach, presented in Section 5, to capture the complex interactions between the crack and the material microstructure motivates us to employ it for the fracture analysis of multilayer ferroelectric actuators. In particular, the objective of this section is to study the crack initiation patterns at the electrode edge.

The theory of the phase-field model is presented in Section 5, where the formulation encodes the asymmetric fracture response in tension and compression. This condition is essential for the simulation of the crack propagation at the electrode edge since high compressive stresses are induced in this region [31, 53].

A schematic of the computational model is presented in Fig. 21. All the material parameters, boundary conditions and loading are presented in detail in [3]. Here we consider three extreme assumptions for the bonding of the ceramic and electrode layers at the bottom boundary. The first model assumes that the ceramic layers and internal electrodes are firmly cofired together, i.e. the fully cofired model. In the second model, the ceramic-

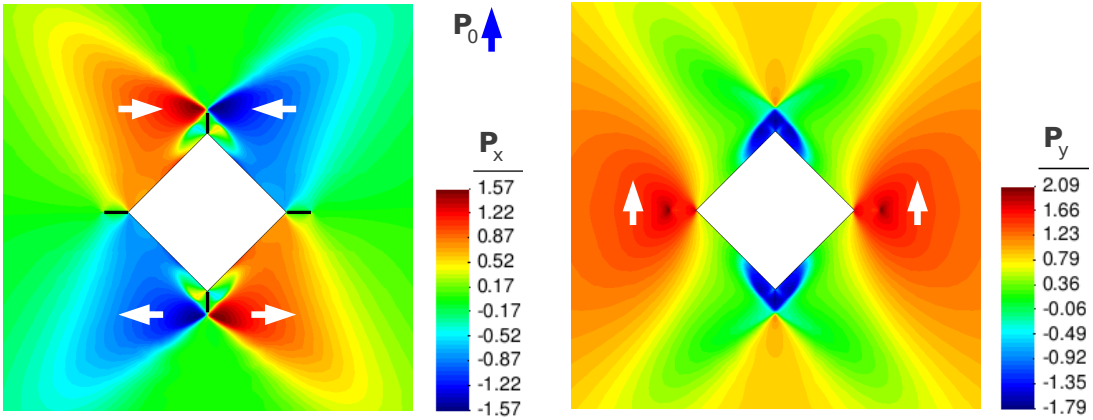

Fig. 20 Snapshot of the microstructure evolution in an area near the indentation. The left and right columns show the horizontal and vertical components of the polarization, respectively. The black lines in the left column indicate the position of the cracks ($v = 0$). The domain orientations are indicated with the white arrows.

electrode interface is considered to be fully cofired while there is no ceramic-ceramic bonding ahead of the electrode edge [146]. This model is called the partially cofired model. Finally, the third assumption considers fully separated layers on both interfaces, representing a single layer of the multilayer actuator where the internal electrode is located at the surface of the actuator [72]. This model is called the surface electrode model.

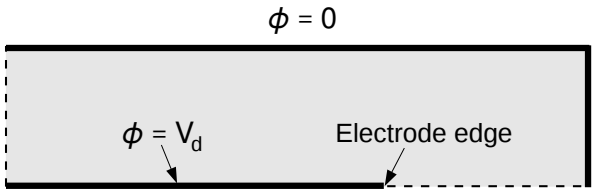

Fig. 21 Schematic of the computational model for a single layer of the multilayer actuator. The electrodes are indicated with the thick lines. V_d is the driving voltage of the actuator.

Figure 22 presents snapshots of the crack propagation in a small neighborhood of the electrode edge for the three models. As the driving voltage V_d increases, the crack initiates at the electrode edge and evolves in a different direction from the electrode edge in each model. Figure 22(a) shows that the crack mainly propagates along the ceramic-ceramic interface ahead of the electrode edge in the fully cofired model. On the contrary, Fig. 22(b) indicates that a preferential path for the crack propagation is along the ceramic-electrode interface in the partially cofired model. It is interesting to observe in Fig. 22(c) that the crack propagates obliquely from the electrode into the material in the surface electrode model.

The crack initiation patterns presented in Fig. 22 reflect a crack propagation scenario in multilayer ferroelectric actuators. The ceramic layers and electrodes are fully cofired together in the most common design of these actuators. For this design, the simulation results in Fig. 22(a) show that the ceramic-ceramic interface ahead of the electrode edge is the first crack initiation site. The crack propagation along this interface gradually converts the fully cofired actuator to a partially cofired one. In this situation, the second mode of fracture will be activated, which is the crack initiation along the electrode-ceramic interface, see Fig. 22(b). If the new crack propagates a certain distance along this interface, the partially cofired actuator becomes a surface electrode one, where the crack starts to propagate obliquely into the material, see Fig. 22(c). The above mentioned events can be interpreted as a crack initiation process in multilayer ferroelectric actuators. Interestingly, this mechanism explains the experimental observations, in which the crack is initiated at the internal electrode edge, and it branches basically into three directions from the electrode edge which results in the delamination and oblique cracking of multilayer ferroelectric actuators [8, 31, 117].

7 Phase-field model of fracture in ferroelectric polycrystals

To study the fracture process in ferroelectric polycrystals, the effect of polycrystalline microstructure should be considered by incorporating the different fracture toughness of the bulk and the grain boundaries, and the different crystal orientations of the grains. Related models do not take into account the effects of grain boundaries and grain size [61, 64]. In [120], inter- and

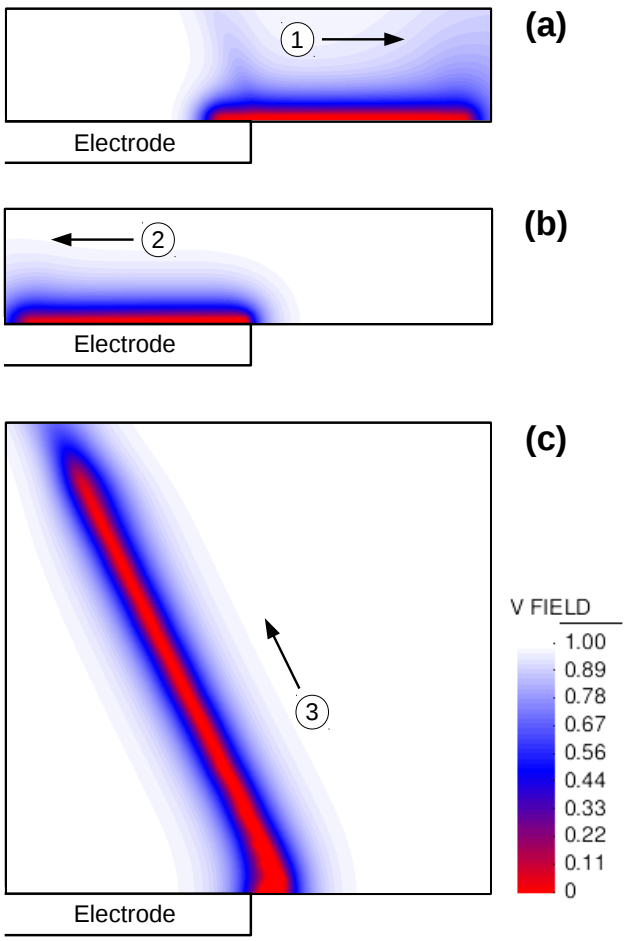

Fig. 22 Crack initiation patterns in a small neighborhood of the electrode edge for the (a) fully cofired, (b) partially cofired, and (c) surface electrode models. The color contour indicates the distribution of v field representing the fracture area. The arrows present the crack propagation directions from the electrode edge. The numbers indicate the sequence of crack initiation events from the fully cofired to the surface electrode model.

transgranular crack propagation is modeled in linear piezoelectric polycrystals, thus not accounting for the effect of ferroelectric domain microstructures. The main objective of this section is to introduce a model for evaluating the effects produced by both the grain and the ferroelectric domain microstructures on the fracture response of the material. For this purpose, we have extended to polycrystals the phase-field model of fracture in ferroelectric single crystals presented in Section 3. This extension is based on two approaches for (1) grain growth [26] to provide realistic polycrystalline microstructures with different grain sizes and (2) ferroelectric polycrystals [145] to introduce different crystal orientations of the grains. The resulting model couples three phase-fields describing (1) the polycrystalline, (2) the location of the cracks, and (3) the ferroelectric domain microstructure [4].

The total free energy of a heterogeneous system is stated in the context of phase-field models as [26]

$$F = \int_{\Omega} [f_0(\eta_1, \eta_2, ..., \eta_m) + \sum_{i=1}^{m} \frac{\kappa_i}{2} (\nabla \eta_i)^2] \, \mathrm{d}\Omega, \tag{17}$$

where f_0 is the local free energy density presented in detail in [26]. κ_i are the gradient energy coefficients and field variables η_i indicate the grains where the minima of f_0 are located at $(\eta_1, \eta_2, ..., \eta_m)$ = (1, 0, ... , 0), (0, 1, ... , 0), ... , (0, 0, ... , 1),(-1, 0, ... , 0), (0, -1, ... , 0), ... , (0, 0, ... , -1). The grain boundaries are the regions of the domain where the gradient energy terms are non-zero. The evolution of the grains is governed by the Ginzburg-Landau equations. The polycrystalline microstructure given by this model is included in the total electromechanical enthalpy in Eq. (11) as follows. The fracture properties of the grain boundaries can be characterized by assuming a lower fracture toughness along these boundaries as compared to the grain interiors [35, 111, 120]. The grain boundaries can be identified through a function ξ of the orientation field variables η_i defined as

$$\xi = \sum_{i=1}^{m} \eta_i^{2k}, \tag{18}$$

where k is a positive integer. The function ξ has a unit value inside the grains and smaller positive values at the grain boundaries. This function makes it possible to assign a lower fracture toughness along the grain boundaries than in the grain interiors. The critical energy release rate in a polycrystal can be defined as [4]

$$G_c^{poly} = G_c \, \mathscr{F}(\xi), \tag{19}$$

where G_c is the critical energy release rate of the bulk crystal, and the function $\mathscr{F}$ controls the weakening of the material at the grain boundaries. The maximum of this function is 1 and its minimum indicates the ratio of the critical fracture energy of the grain boundary to that of the grain interior. This ratio can be regulated by an appropriate selection of the function $\mathscr{F}$ and setting the power k in Eq. (18). Here, the function $\mathscr{F}$ is chosen to be proportional to ξ, i.e. $\mathscr{F}(\xi) = \xi$ and the power of ξ is also assigned as $k = 1$. Each grain is also assumed to be oriented along a different crystallographic direction. We define the rotation angle θ whose value is assigned randomly for each orientation field variables η_i $(i = 1, ..., m)$. Using the orientation field and following the phase-field model of ferroelectric polycrystals [145], the electromechanical enthalpy density $\mathcal{H}$ in Eq. (9) can

be extended to polycrystals. For this purpose, each of the energy terms in Eq. (9) is transformed from the local coordinate system of each individual grain to the global coordinate system of the polycrystal, θ being the angle between these two coordinate systems. It can be shown that all the energy terms except χ remain unchanged by this transformation. The modified energy density χ^{poly} is presented in [4]. By replacing the modified χ^{poly} and G_c^{poly} in Eq. (11), the electromechanical enthalpy density for a ferroelectric polycrystal takes the form [4]

$$\begin{aligned}\mathcal{H}^{poly}(\boldsymbol{\varepsilon}, \mathbf{p}, \nabla\mathbf{p}, \mathbf{E}, v) = (v^2 + \eta_\kappa)\,[U(\nabla\mathbf{p}) + W(\mathbf{p}, \boldsymbol{\varepsilon})] \\ + \chi^{poly}(\mathbf{p}) - \frac{\varepsilon_0}{2}|\mathbf{E}|^2 - \mathbf{E}\cdot\mathbf{p} \\ + G_c^{poly}\left[\frac{(1-v)^2}{4\kappa} + \kappa|\nabla v|^2\right].\end{aligned} \tag{20}$$

The time evolution of the system along with a solution algorithm are presented in [4].

To perform numerical simulations, a rectangular domain is considered. First, the phase-field model of grain growth is used to obtain different polycrystalline microstructures. Two snapshots of the polycrystalline microstructure evolution are presented in Fig. 23(a) and (b). The contour of ξ in Eq. (18) is depicted in these figures. Grain boundaries are highlighted by darker regions. These two polycrystalline microstructures are selected for the fracture simulations in a fine- and a coarse-grain ferroelectric polycrystal, respectively.

For the fracture simulations, a monotonically increasing mechanical load is applied by pulling the top and bottom sides of the model with a uniform vertical mechanical displacement. All the material parameters are selected to fit the behavior of single crystals of barium titanate ($BaTiO_3$). Figures 23(a) and (b) present the final computed crack paths (when the sample is splitted into two parts) in the fine- and coarse-grain structures, respectively. It is obvious in Fig. 23(a) that the crack propagates mainly along the grain boundaries, demonstrating the intergranular mode of fracture in the fine-grain structure. On the other hand, transgranular crack propagation is observed in Fig. 23(b) where the crack propagates through the grains. This transition from intergranular fracture for small grains to transgranular fracture in the case of large grains has been observed in experiments [55, 80].

The evolution of the normalized surface energy (the integral of the last term in Eq. (20)) is plotted in Fig. 24 as a function of the load step w for the fine- and coarse-grain structures. Both graphs are almost identical until the cracks initiate at load step $w = 1.17$. After the initiation, the crack in the fine-grain structure starts to

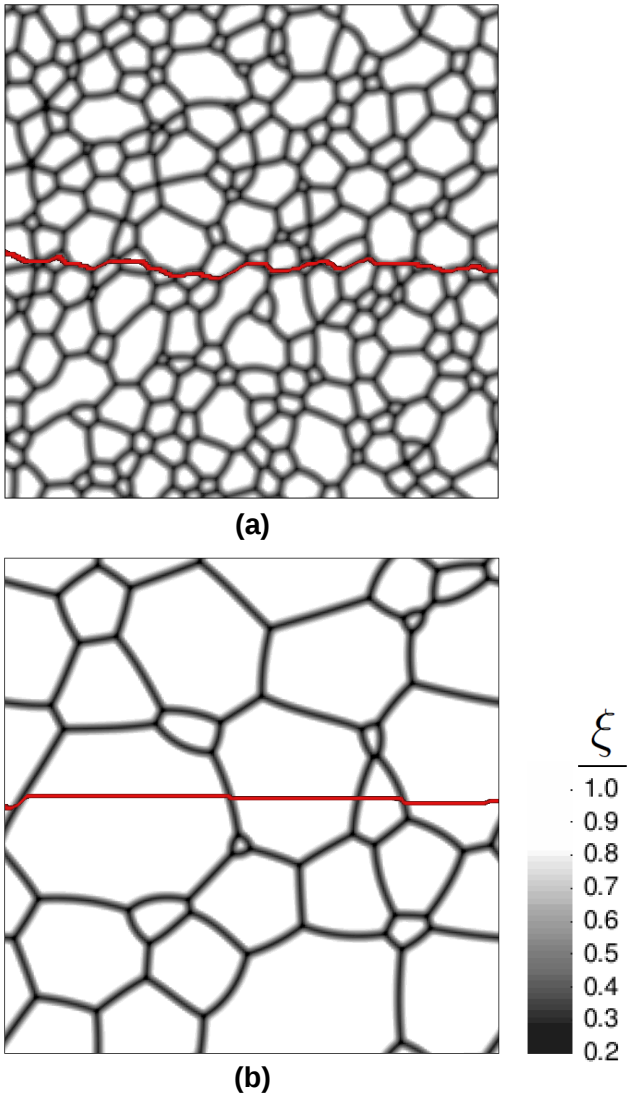

Fig. 23 Crack path in (a) fine-grain and (b) coarse-grain ferroelectric polycrystals. The points where $v = 0$ are depicted in red to indicate the crack position. The gray contour indicates the distribution of ξ. Grain boundaries are highlighted by darker regions.

propagate abruptly along the grain boundaries, i.e. a small increase of the load leads to a big jump in the surface energy. This is due to the lower fracture toughness of the grain boundaries. Interestingly, the abrupt propagation stops at load step $w = 1.2$ (point **a** in the fine-grain graph). Simulation results show that this crack arrest is due to crack deflection along the grain boundary [4]. This phenomena is the so-called crack deflection toughening in intergranular mode of fracture [25, 58]. The crack shows this behavior in other load steps **b** and **c**, marked in the fine-grain graph of Fig. 24.

The graph of the coarse-grain microstructure in Fig. 24 shows a slower growth rate than the fine-grain structure. The transgranular mode of fracture in the coarse-

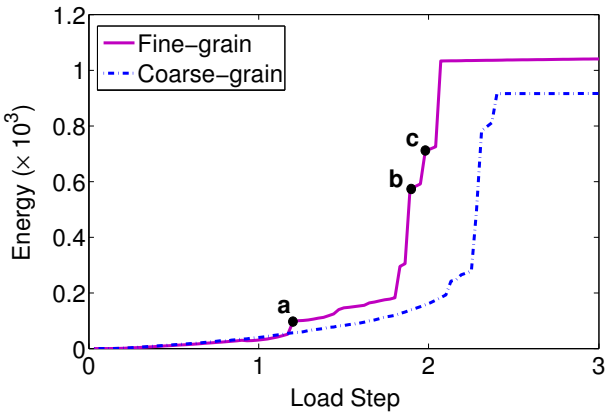

Fig. 24 Evolution of the normalized surface energy as a function of the load step.

grain structure allows the crack to interact with the ferroelectric domain microstructure inside the grains. The polarization vectors start to rotate towards the vertical direction around the fracture zone due to the high tensile stresses, leading to 90^o ferroelastic domain switching mentioned in Section 3. Therefore, domain switching-induced toughening is the main toughening mechanism in the coarse-grain ferroelectric polycrystal. In contrast, this mechanism is less pronounced in the fine-grain structure. This is due to the fact that the tensile stresses around the crack are smaller in the fine-grain structure since the crack propagates faster along the grain boundaries with a lower applied load. Therefore, 90^o ferroelastic switching is less favorable in the fine-grain structure. Consequently, the effective fracture toughness of the coarse-grain structure is higher than the fine-grain, in agreement with experiments [80].

8 Conducting crack propagation driven by electric fields in ferroelectric ceramics

Several experiments have reported electric-field induced crack growth of ferroelectric ceramics from insulating notches [50, 73, 74, 76, 105, 128, 129]. However, related theoretical approaches show that electric field loading, perpendicular to an insulating crack, decreases the total energy release rate, i.e. electric fields retard the crack propagation [62, 66, 77, 78, 86, 100, 113]. This discrepancy indicates that the induced strain incompatibility around the notch is the main cause of crack propagation rather than electrostatic forces. In contrast, electric fields parallel to a conducting crack increase the total energy release rate, which enhance the crack propagation [92, 100, 113, 114, 137]. Experiments on conducting cracks also show the fracture of ferroelectric ceramics under purely electrical loading [13, 29, 140, 141, 142, 143]. Most of these experimental results imply that the major driving force to propagate the conducting cracks is the electrostatic force due to the accumulation of charges with the same sign at the crack tip. The fracture behavior of conducting cracks has been also investigated under combined mechanical and electrical loads [33, 45].

The nonlinear effects of the domain switching in ferroelectrics have not been considered in the above mentioned models for the conducting cracks since they are based on simplified electrostrictive or linear piezoelectricity theories. These effects have been taken into account in other approaches to investigate the toughening of conducting cracks due to domain switching [14, 49, 93]. However, these models are unable to study the crack propagation mechanisms in ferroelectric ceramics since they assume fixed crack configurations. We have presented a model, extending the phase-field theory proposed in Section 5 to model conducting crack propagation in ferroelectric ceramics and investigating the crack propagation mechanisms under purely electrical loading [6]. This section presents a summary of this work.

In the framework of sharp-crack models, a conducting crack is equivalent to assuming that the crack surfaces are coated with perfectly conducting electrode. Therefore, the electric potential all over the crack is constant and the electric field inside the crack gap is zero. This condition can also be obtained by filling the crack gap with a conducting fluid or electrolyte such as NaCl solution [33, 45] or silver paint [141, 142]. The crack-gap filling electrolyte resembles an internal conducting layer with infinite permittivity. In the context of phase-field models, this layer can be defined in a smeared way by multiplying the vacuum permittivity ε_0 by the jump set function $1/(v^2 + \varepsilon_c^{-1})$, where ε_c is the relative permittivity of the fractured zone. The jump set function attains its maximum for $v = 0$, inside the fractured zone, encoding the conditions of a conducting layer with a sufficient large value for the relative permittivity ε_c. On the other hand, this function does not alter the vacuum permittivity outside of the fracture zone ($v = 1$) since ε_c^{-1} is an infinitesimal value. A schematic of a diffuse conducting layer is shown in Fig. 25. The smooth transition between the insulating vacuum and conducting layers ($0 < v < 1$) represents a semi-conducting layer. This transition becomes sharper and the semi-conducting layer tends to disappear when the regularization parameter κ tends to zero. By introducing the diffuse conducting layer, the electromechanical enthalpy density in Eq. (16) is modified for a conducting crack as [6]

$$W_f(\boldsymbol{\varepsilon}, \mathbf{p}, \phi, v) = (v^2 + \eta_\kappa)[U(\nabla \mathbf{p}) + W_c(\mathbf{p}, \boldsymbol{\varepsilon})] + \chi(\mathbf{p}) + \nabla\phi \cdot \mathbf{p} - \frac{1}{(v^2 + \varepsilon_c^{-1})} \frac{\varepsilon_0}{2} |\nabla\phi|^2, \quad (21)$$

It can be seen that, in the limit of vanishingly small regularization parameter, the proposed phase-field model recovers the conditions of the sharp conducting crack. Note that this formulation together with the energy density W_e in Eq. (15) account for the asymmetric behavior in tension and compression and encode also the free-polarization conditions, as discussed in Section 5. The governing equations, material parameters and a solution algorithm are presented in [2].

To perform numerical simulations, we consider a square domain with a conducting pre-notch. The initial polarization is along the positive horizontal direction, parallel to the pre-notch. The electric potential is fixed to zero on the notch surface. An electric field of up to E = 1.4 KV/mm is applied incrementally in the positive and negative horizontal directions. Figure 26 presents two snapshots of the crack propagation under the positive and negative electric fields. As the electric field increases, the cracks start to propagate in two directions from the notch tip. The cracks under the positive field are more curved and tend to branch again by increasing the load. Interestingly, an oblique crack propagation is also observed in experiments of conducting cracks in ferroelectric ceramics under purely electrical loading [142]. Our simulation results in Fig. 26 also show that the cracks are longer under the negative electric field which is in agreement with experiments, showing that electric fields in opposite to the initial polarization strongly facilitate the conducting fracture [33].

The observed crack patterns in Fig. 26 are due to the domain switching during crack growth. Snapshots of the domain evolution under positive and negative electric fields are presented in Fig. 27. The formation of tail-to-tail and head-to-head 90^o domains is obvious in Figs. 27(a) and (b), respectively, leading to charge accumulation around the cracks. This charge accumulation with the same sign induces a high electric field at the crack tip, which in turn leads to a large electrostatic energy (last term in Eq. (21)) for driving the crack. Figure 26(a) also shows the nucleation of small crack branches which is due to the formation of new twins under the positive electric field, see Fig. 27(a).

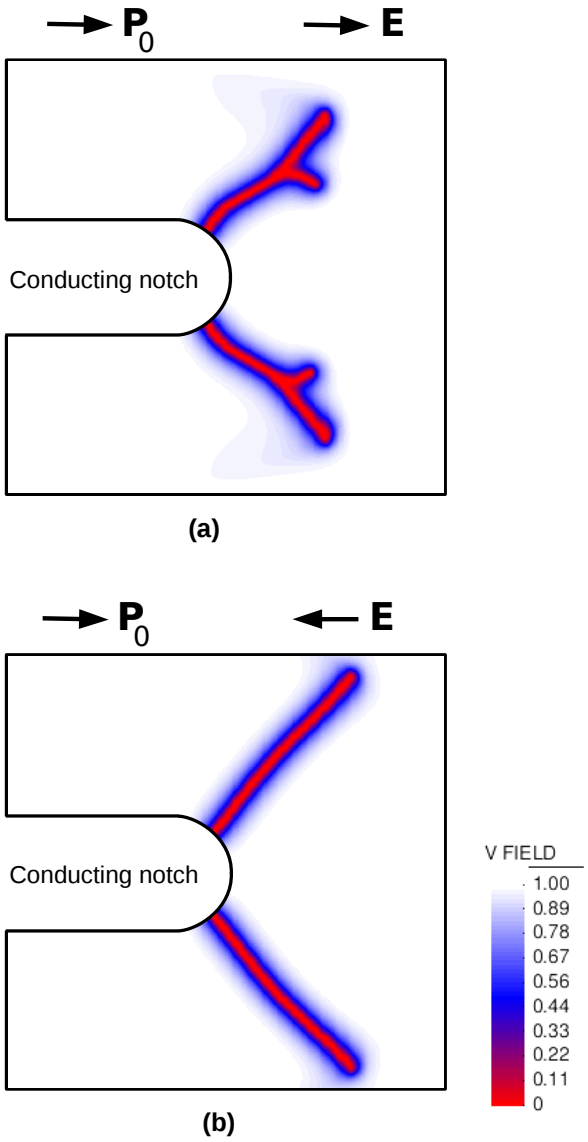

Fig. 26 Snapshots of the fracture evolution: contour plots of the field v under (a) positive and (b) negative electric fields.

9 Numerical simulation of 3-D crack propagation in ferroelectric single crystals

We extend the phase-field model of fracture in ferroelectric single crystals proposed in Section 3 to three dimensions for a more precise evaluation of the microstructure effect on the crack propagation. Here we consider a traction-free, free-polarization and permeable crack. The electro-mechanical enthalpy density of a possibly fractured ferroelectric for these conditions is stated in Eq. (9). Following [110], the energy functions U, W and χ are expanded in terms of three-dimensional components as

$$U(p_{i,j}) = \frac{a_0}{2}(p_{1,1}^2 + p_{2,2}^2 + p_{3,3}^2 + p_{1,2}^2 + p_{2,1}^2) + \frac{a_0}{2}(p_{1,3}^2 + p_{3,1}^2 + p_{2,3}^2 + p_{3,2}^2), \quad (22)$$

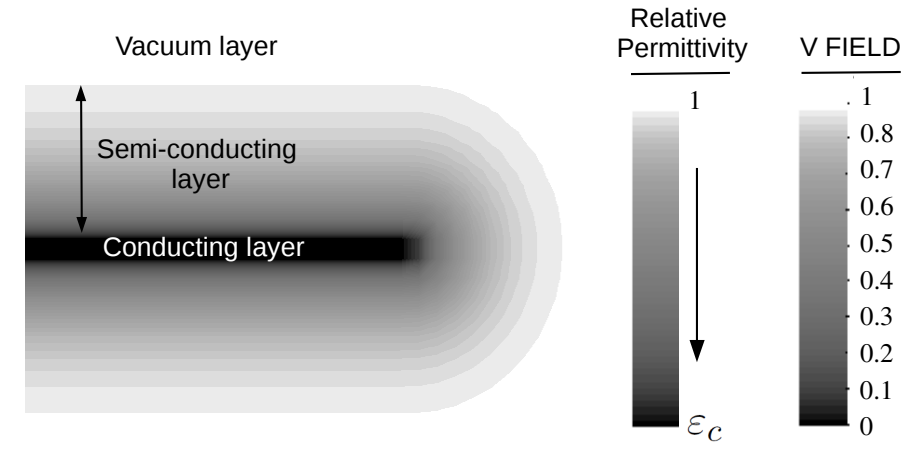

Fig. 25 Schematic of a diffuse conducting layer.

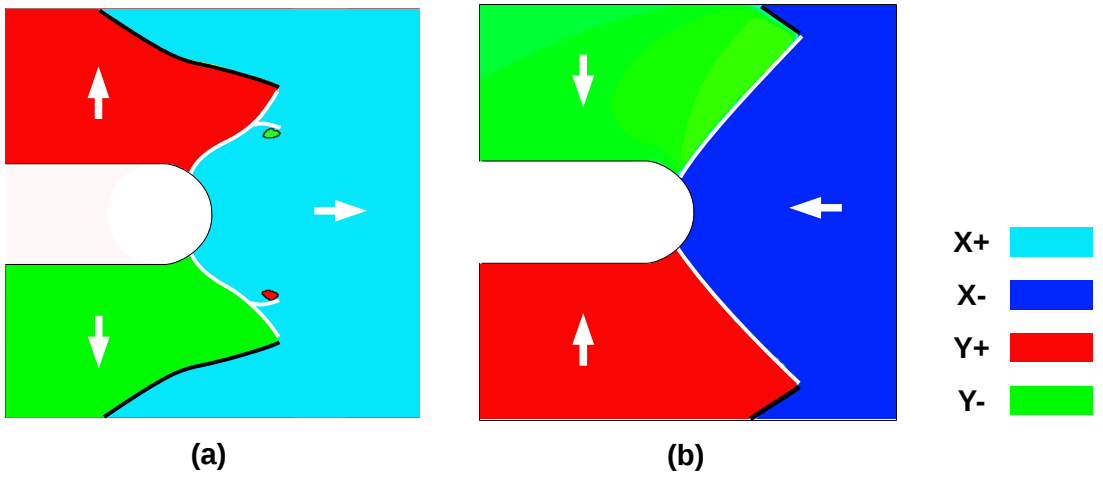

Fig. 27 Snapshots of the microstructure evolution under (a) positive and (b) negative electric fields with a magnitude of $|E| = 1.4$ KV/mm. The white lines indicate the position of the cracks ($v = 0$). Domain walls are represented by the thick black lines. There are four tetragonal variants, labeled as X+, X-, Y+, and Y- with components of the normalized polarization $(p_1' > \tau)$, $(p_1' < -\tau)$, $(p_2' > \tau)$, and $(p_2' < -\tau)$, respectively. The value of τ is chosen as 20% of the normalized spontaneous polarization, i.e. $\tau = 0.2$. The four tetragonal variants are colored according to the legend.

$$
\begin{aligned}
W(p_i,\varepsilon_{jk}) = &-\frac{b_1}{2}(\varepsilon_{11}p_1^2+\varepsilon_{22}p_2^2+\varepsilon_{33}p_3^2)\\
&-\frac{b_2}{2}\left((\varepsilon_{22}+\varepsilon_{33})p_1^2+(\varepsilon_{11}+\varepsilon_{33})p_2^2+(\varepsilon_{11}+\varepsilon_{22})p_3^2\right)\\
&-b_3\left((\varepsilon_{12}+\varepsilon_{21})p_1p_2+(\varepsilon_{13}+\varepsilon_{31})p_1p_3\right)\\
&-b_3\left((\varepsilon_{23}+\varepsilon_{32})p_2p_3\right)+\frac{c_1}{2}(\varepsilon_{11}^2+\varepsilon_{22}^2+\varepsilon_{33}^2)\\
&+c_2(\varepsilon_{11}\varepsilon_{22}+\varepsilon_{11}\varepsilon_{33}+\varepsilon_{22}\varepsilon_{33})\\
&+\frac{c_3}{2}(\varepsilon_{12}^2+\varepsilon_{21}^2+\varepsilon_{13}^2+\varepsilon_{31}^2+\varepsilon_{23}^2+\varepsilon_{32}^2),
\end{aligned}
\tag{23}
$$

$$
\begin{aligned}
\chi(p_i) = &\frac{a_1}{2}(p_1^2+p_2^2+p_3^2)+\frac{a_2}{4}(p_1^4+p_2^4+p_3^4)\\
&+\frac{a_3}{2}(p_1^2p_2^2+p_2^2p_3^2+p_1^2p_3^2)\\
&+\frac{a_4}{6}(p_1^6+p_2^6+p_3^6)\\
&+\frac{a_5}{4}(p_1^4p_2^4+p_2^4p_3^4+p_1^4p_3^4),
\end{aligned}
\tag{24}
$$

where all of the variables and parameters are defined in Section 3. The governing equations, solution algorithm and normalizations are also presented in Section 3. The normalized parameters for barium titanate ($BaTiO_3$) are given in Table 5.

For numerical simulations, a cubic domain is considered with the boundary conditions depicted in Fig. 28. The normalized dimensions of the domain are $200\times200\times200$ and it is discretized with approximately 6,000,000 tetrahedral finite elements of size $h \simeq 2$. A monotonically increasing mechanical load is applied by pulling the top

Table 5 Normalized parameters

c_1'	c_2'	c_3'	b_1'	b_2'	b_3'	a_0'
185	111	74	1.4282	-0.185	0.8066	0.02
a_1'	a_2'	a_3'	a_4'	a_5'	ε_0'	G_c'
-0.007	-0.009	0.018	0.0261	5	0.131	15.6

and bottom faces of the model with a uniform mechanical displacement such that $\mathbf{u}_{\pm} = (0, \pm w, 0)$, where + and - indicate the top and bottom faces of the model, respectively, and w is the load step. To facilitate the crack initiation, the x_2 component of mechanical displacement is also constrained at the top half and bottom half of the front face highlighted with yellow such that $u_{2\pm} = \pm w$. To avoid the compression of the model, the x_3 component of mechanical displacement is fixed on the right (highlighted with green) and left faces. The initial polarization $\mathbf{p}_{init} = (1, 0, 0)$ is assigned along the positive x_1 direction, see Fig. 28. As for the electrical boundary conditions, the electric potential on the front (yellow) and back faces is set to 0. It is also assumed that the normal component of the electric displacement vanishes on other faces and they satisfy the free-polarization boundary conditions. We follow a solution algorithm presented in [1]. One hundred load increments are performed in the simulation with an increment of $\Delta w = 5 \times 10^{-2}$. The simulations are carried out on parallel processors using the finite element library of the Kratos multi-physics package [19].

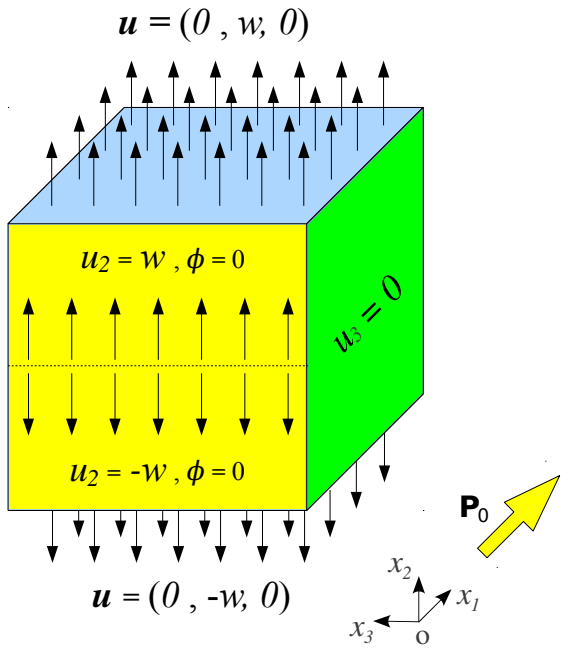

Fig. 28 3-D computational model with boundary conditions.

Figure 29 presents four snapshots of the evolution of the microstructure and the crack. The left column shows the field v representing the fractured area and the right column shows the polarization magnitude $|\mathbf{p}|$, which highlights the domain structure. These figures indicate a similar interaction of the crack and ferroelectric domains reported in Section 3 but in this case in three dimensions. This interaction leads to the slow-fast crack propagation behavior. The snapshots in Fig. 29(b), (c), and (d) correspond to slow propagation periods arrested by the twins ahead of the crack represented with bold white arrows. These preliminary results verify the formulation and implementation of the 3-D model. Using this model, we have addressed computationally the complexity of the intrinsically 3-D fracture mechanisms, and in this way have examined the commonly perceived toughening mechanisms in these materials without including them a priori into the model [7].

10 Conclusions

This section summarizes the main contributions and research ideas of the paper. We have presented simulations of the fully coupled interaction between the crack propagation and the formation and evolution of microstructure in ferroelectric materials. For this purpose, a family of phase-field models has been introduced in this paper which is outlined as follows:

- *A phase-field model for the coupled nucleation and evolution of cracks and domains in ferroelectric single crystals* [1]: The model naturally couples two energetic phase-field models for fracture and for the microstructure of ferroelectric single crystals. We have exercised the model in plane polarization and plane strain simulations of a sample under either mechanical or combined electro-mechanical loading conditions.
- *Phase-field models to encode various electromechanical crack-face boundary conditions* [5]: These models are based on a variational formulation of brittle fracture coupled with the linear theory of piezoelectricity and a phase-field model of ferroelectric domain evolution. This coupling encodes various electromechanical crack-face boundary conditions of a sharp-crack into the phase-field framework. We have performed a set of simulations to compare the results of the proposed models with that of the corresponding sharp-crack models.
- *A developed phase-field model to explain anisotropic crack growth in ferroelectrics* [2]: The model has been developed by introducing a crack non-interpenetration condition in the variational approach to fracture accounting for the asymmetric behavior in tension and compression. We have exercised the model under the Vickers indentation loading and during the poling process of multilayer ferroelectric actuators.
- *A phase-field model to simulate intergranular and transgranular crack propagation in ferroelectric polycrystals* [4]: The proposed phase-field model for fer-

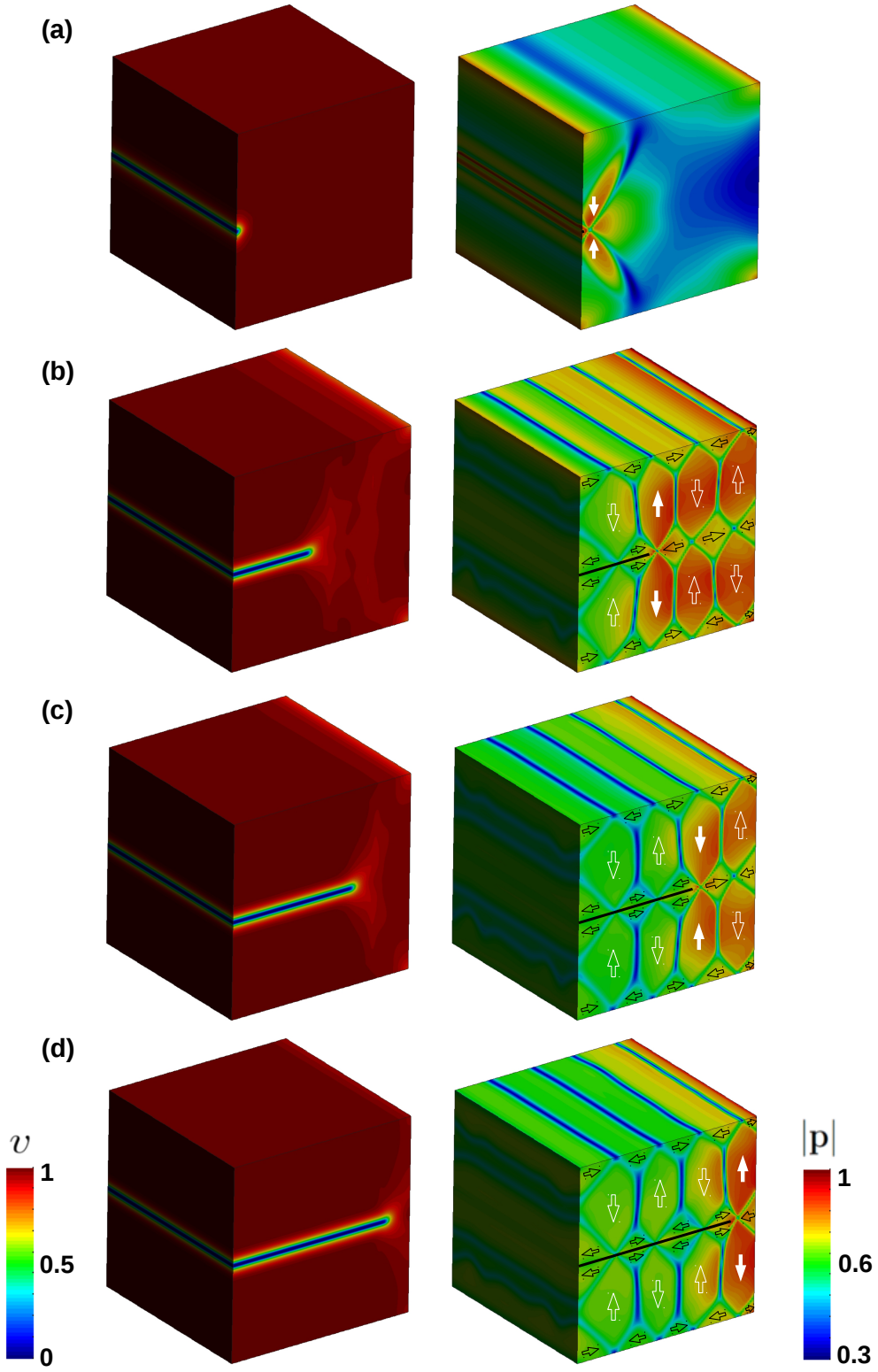

Fig. 29 Four snapshots of the evolution of the microstructure and the permeable crack at load steps (a) $w = 1.5$, (b) $w = 4.35$, (c) $w = 4.55$, (d) $w = 4.65$. The left column shows the field v representing the fractured area, and the right column shows the polarization magnitude $|\mathbf{p}|$, which highlights the domain structure. Domain orientations are indicated with arrows, which are bold white for the twins ahead of the crack. The points where $v = 0$ are represented in black in the polarization maps to show the crack position.

roelectric single crystals has been extended to polycrystals by incorporating the different fracture toughness of the bulk and the grain boundaries, and the different crystal orientations of the grains. We have exercised the model with fine- and coarse-grain microstructures.

- *A developed phase-field model to simulate conducting crack propagation driven by electric fields* [6]: The model has been developed by introducing the electrical enthalpy of a diffuse conducting layer into the phase-field formulation of fracture in ferroelectric single-crystals. We have exercised the model under purely electrical loading.

The main simulation results of the proposed models, in agreement with experimental observations, are summarized in the following:

- The interaction of the microstructure and the crack leads to a slow-fast crack propagation behavior in ferroelectric single crystals [1, 27].
- 90^o domain switching induced by an intense crack-tip stress field is the major mechanism behind the fracture toughening effect in ferroelectric materials [1, 80, 81].
- An enhanced crack propagation is obtained for parallel cracks under applied electric fields with the coercive magnitude [1, 101].
- Radial cracks perpendicular to the poling direction of the material propagate faster than parallel ones [2, 75, 89, 101, 112, 116, 121].
- Cracks propagate mainly along the grain boundaries in fine-grain ferroelectric polycrystals, demonstrating the intergranular mode of fracture. On the other hand, transgranular crack propagation is observed in coarse-grain microstructures where cracks propagate through the grains [4, 55, 80].
- Crack deflection is shown as the main toughening mechanism in the fine-grain microstructures [4, 25, 58]. Due to the ferroelectric domain switching mechanism, noticeable fracture toughness enhancement is also obtained for transgranular crack propagation and the effective fracture toughness of the coarse-grain microstructures is observed to be higher than the fine-grain [4, 80].
- A negative electric field (below the coercive field) enhances the crack propagation perpendicular to the initial polarization in ferroelectrics, while a positive electric field retards it [5, 50, 95, 106, 121].
- An oblique crack propagation and crack branching from a conducting notch is observed in a ferroelectric sample under purely electrical loading [6, 142]. A negative electric field induces a larger driving force with respect to the positive one [6, 33].
- Different crack initiation patterns are observed at electrode edges in multilayer ferroelectric actuators. The obtained patterns can be interpreted as initiation sources of experimentally observed crack branches near the electrode edge [3, 8, 31, 117].

The works summarized in this paper also leave some open research lines for the future. We suggest the following lines:

- Experimental observations in poled $BaTiO_3$ single crystal specimens reveal that the crack propagates along the orthogonal walls of 90^o domains , following a zig-zag path that matches the domain pattern [27]. This can be included in our model by considering a lower surface energy or fracture toughness along the orthogonal walls.
- A more precise evaluation of the microstructure effect will be obtained by running longer simulations producing more extended cracks.
- The model of fracture in ferroelectric polycrystals presents three lengthscales: (1) the width of the grain boundaries, (2) the width of the ferroelectric domain walls, and (3) the width of the smeared cracks. The latter is a numerical artifact, controlled by the regularization parameter of the fracture phase-field. A sensitivity analysis on this parameter relative to the other lengthscales of the problem would be necessary, since the width of the smeared crack has a significant effect on the simulation results. In addition, for more realistic fracture simulations of ferroelectric polycrystals, the relative physical size of the grains and ferroelectric domains should be considered.
- Dielectric breakdown often occurs via the formation of conducting tubular channels around electrodes and conducting cracks. The tubular channels can have an important effect on the electromechanical fields and the microstructure of the material. The propagation of the tubular channels can be modeled in a similar way to that of the conducting cracks.

Acknowledgements The authors gratefully acknowledge the support of the Ministerio de Ciencia e Innovación (DPI2011-26589).

References

1. Abdollahi A, Arias I (2011) Phase-field modeling of the coupled microstructure and fracture evolution in ferroelectric single crystals. Acta Mater 59(12):4733–4746

2. Abdollahi A, Arias I (2011) Phase-field simulation of anisotropic crack propagation in ferroelectric single crystals: effect of microstructure on the fracture process. Model Simul Mater Sci Eng 19(7):074,010
3. Abdollahi A, Arias I (2012) Crack initiation patterns at electrode edges in multilayer ferroelectric actuators. Smart Mater Struct 21(9):094,011
4. Abdollahi A, Arias I (2012) Numerical simulation of intergranular and transgranular crack propagation in ferroelectric polycrystals. Int J Fract 174(1):3–15
5. Abdollahi A, Arias I (2012) Phase-field modeling of crack propagation in piezoelectric and ferroelectric materials with different electromechanical crack conditions. J Mech Phys Solids 60:2100–2126
6. Abdollahi A, Arias I (2013) Conducting crack propagation driven by electric fields in ferroelectric ceramics. Acta Mater 61(19):7087–7097
7. Abdollahi A, Arias I (2013) Three-dimensional simulation of crack propagation in ferroelectric polycrystals: effect of combined toughening mechanisms Submitted for publication
8. Aburatani H, Harada S, Uchino K, Furuta A, Fuda Y (1994) Destruction mechanisms in ceramic multilayer actuators. JPN J Appl Phys 1 33:3091–3094
9. Amor H, Marigo JJ, Maurini C (2009) Regularized formulation of the variational brittle fracture with unilateral contact: Numerical experiments. J Mech Phys Solids 57(8):1209–1229
10. Arias I, Serebrinsky S, Ortiz M (2006) A phenomenological cohesive model of ferroelectric fatigue. Acta Mater 54(4):975–984
11. Benes M, Chalupecky V, Mikula K (2004) Geometrical image segmentation by the Allen-Cahn equation. Appl Numer Math 51(2-3):187–205
12. Beom HG, Atlurib SN (2003) Effect of electric fields on fracture behavior of ferroelectric ceramics. J Mech Phys Solids 51:1107–1125
13. Beom HG, Jeong KM, Park JY, Lin S, Kim GH (2009) Electrical failure of piezoelectric ceramics with a conductive crack under electric fields. Eng Fract Mech 76:2399–2407
14. Beom HK, Youn SK (2004) Electrical fracture toughness for a conducting crack in ferroelectric ceramics. Int J Solids Struct 41(1):145–157
15. Bourdin B (2007) Numerical implementation of the variational formulation for quasi-static brittle fracture. Interfaces Free Bound 9:411–430
16. Bourdin B, Francfort GA, Marigo JJ (2000) Numerical experiments in revisited brittle fracture. J Mech Phys Solids 48(4):797–826
17. Bourdin B, Francfort GA, Marigo JJ (2008) The variational approach to fracture. J Elast 91(1-3):5–148
18. Camacho GT, Ortiz M (1996) Computational modelling of impact damage in brittle materials. Int J Numer Methods Eng 33(20-22):2899–2938
19. Dadvand P, Rossi R, Onate E (2010) An object-oriented environment for developing finite element codes for multi-disciplinary applications. Arch Comput Methods Eng 17(3):253–297
20. Dayal K, Bhattacharya K (2007) A real-space non-local phase-field model of ferroelectric domain patterns in complex geometries. Acta Mater 55(6):1907–1917
21. Deeg WFJ (1980) The analysis of dislocation, crack, and inclusion problems in piezoelectric solids. PhD thesis, Stanford University
22. Devonshire AF (1949) Theory of barium titanate .1. Philos Mag 40(309):1040–1063
23. Devonshire AF (1951) Theory of barium titanate .2. Philos Mag 42(333):1065 –1079
24. Elhadrouz M, Zineb TB, Patoor E (2006) Finite element analysis of a multilayer piezoelectric actuator taking into account the ferroelectric and ferroelastic behaviors. Int J Eng Sci 44:996–1006
25. Faber KT, Evans AG (1983) Intergranular crack-deflection toughening in silicon-carbide. J Am Ceram Soc 66(6):C94–C96
26. Fan D, Chen LQ (1997) Computer simulation of grain growth using a continuum field model. Acta Mater 45(2):611–622
27. Fang D, Jiang Y, Li S, Sun CT (2007) Interactions between domain switching and crack propagation in poled BaTiO3 single crystal under mechanical loading. Acta Mater 55(17):5758–5767
28. Francfort GA, Marigo JJ (1998) Revisiting brittle fracture as an energy minimization problem. J Mech Phys Solids 46(8):1319–1342
29. Fu R, Zhang TY (2000) Effects of an electric field on the fracture toughness of poled lead zirconate titanate ceramics. J Am Ceram Soc 83(5):1215–1218
30. Fu R, Qian CF, Zhang TY (2000) Electrical fracture toughness for conductive cracks driven by electric fields in piezoelectric materials. Appl Phys Lett 76(1):126–128
31. Furuta A, Uchino K (1993) Dynamic observation of crack-propagation in piezoelectric multilayer actuators. J Am Ceram Soc 76:1615–1617
32. Gao HJ, Zhang TY, Tong P (1997) Local and global energy release rates for an electrically yielded crack in a piezoelectric ceramic. J Mech

Phys Solids 45(4):491–510
33. Gehrig F, Jelitto H, Schneider GA (2008) Fracture criterion for a conducting crack in poled PZT-PIC 151 investigated by stable crack growth. Acta Mater 56(2):222–229
34. Gong X, Suo Z (1996) Reliability of ceramic multilayer actuators: A nonlinear finite element simulation. J Mech Phys Solids 44:751–769
35. Grah M, Alzebdeh K, Sheng PY, Vaudin MD, Bowman KJ, Ostoja-Starzewski M (1996) Brittle-intergranular failure in 2D microstructures: Experiments and computer simulations. Acta Mater 44(10):4003–4018
36. Griffith AA (1921) The phenomena of rupture and flow in solids. Philos Trans Royal Soc London Series A-221:163–198
37. Gu H, Wang J (2013) The influence of crack face electrical boundary conditions on the nonlinear behavior of ferroelectric single crystal. Smart Mater Struct 22(6)
38. Guo XH, Fang DN, Soh AK, Kim HC, Lee JJ (2006) Analysis of piezoelectric ceramic multilayer actuators based on an electro-mechanical coupled meshless method. Acta Mech Sinica 22:34–39
39. Hackemann S, Pfeiffer W (2003) Domain switching in process zones of pzt: characterization by microdiffraction and fracture mechanical methods. J Eur Ceram Soc 23(1):141–151
40. Hakim V, Karma A (2009) Laws of crack motion and phase-field models of fracture. J Mech Phys Solids 57(2):342–368
41. Han X, Li X, Mao SX (2002) Toughening and weakening in ferroelectric ceramics by domain-switching process under mixed electric and mechanical loading. Metall Mater Trans A 33(9):2835–2845
42. Hao TH, Shen ZY (1994) A new electric boundary-condition of electric fracture-mechanics and its applications. Eng Fract Mech 47(6):793–802
43. Hao TH, Gong X, Suo Z (1996) Fracture mechanics for the design of ceramic multilayer actuators. J Mech Phys Solids 44:23–48
44. Haug A, McMeeking RM (2006) Cracks with surface charge in poled ferroelectrics. Eur J Mech A-Solids 25(1):24–41
45. Heyer V, Schneider GA, Balke H, Drescher J, Bahr HA (1998) A fracture criterion for conducting cracks in homogeneously poled piezoelectric PZT-PIC 151 ceramics. Acta Mater 46(18):6615–6622
46. Huber JE (2005) Micromechanical modelling of ferroelectrics. Curr Opin Solid State Mater Sci 9(3):100–106
47. Hwang SC, Lynch CS, McMeeking RM (1995) Ferroelectric/ferroelastic interactions and a polarization switching model. Acta Mater 43(5):2073–2084
48. Jacqmin D (1999) Calculation of two-phase Navier-Stokes flows using phase-field modeling. J Comput Phys 155(1):96–127
49. Jeong KM, Beom HG (2004) Conducting crack growth in ferroelectric ceramics subjected to electric loading. Smart Mater Struct 13(2):275
50. Jiang Y, Zhang Y, Liu B, Fang D (2009) Study on crack propagation in ferroelectric single crystal under electric loading. Acta Mater 57:1630–1638
51. Jones LJ, Motahari SM, VarliogIU M, Lienert U, Bernier JV, Hoffman M, Uestuendag E (2007) Crack tip process zone domain switching in a soft lead zirconate titanate ceramic. Acta Mater 55(16):5538–5548
52. Kamlah M (2001) Ferroelectric and ferroelastic piezoceramics - modeling of electromechanical hysteresis phenomena. Contin Mech Thermodyn 13(4):219–268
53. Kamlah M, Bohle U (2001) Finite element analysis of piezoceramic components taking into account ferroelectric hysteresis behavior. Int J Solids Struct 38:605–633
54. Kanzig W (1957) Ferroelectrics and antiferroelectrics. In: Seitz F, Das TP, Turnbull D, Hahn EL (eds) Solid State Physics, Academic Press, p 5
55. Kim SB, Kim DY, Kim JJ, Cho SH (1990) Effect of grain-size and poling on the fracture mode of lead zirconate titanate ceramics. J Am Ceram Soc 73:161–163
56. Koh JH, Jeong SJ, Ha MS, Song JS (2004) Electric field induced fracture mechanism and aging of piezoelectric behavior in Pb(MgNb)O-3-Pb(ZrTi)O-3 multilayer ceramic actuators. Ceram Int 30:1863–1867
57. Krill CE, Chen LQ (2002) Computer simulation of 3-D grain growth using a phase-field model. Acta Mater 50(12):3057–3073
58. Kueck AM, Kim DK, Ramasse QM, De Jonghe LC, Ritchie RO (2008) Atomic-resolution imaging of the nanoscale origin of toughness in rare-earth doped SiC. Nano Lett 8:2935–2939
59. Kuna M (2010) Fracture mechanics of piezoelectric materials - where are we right now? Eng Fract Mech 77(2):309–326
60. Landau L (1937) On the theory of phase transitions. Gordon and Breach
61. Landis CM (2003) On the fracture toughness of ferroelastic materials. J Mech Phys Solids 51:1347–1369

62. Landis CM (2004) Energetically consistent boundary conditions for electromechanical fracture. Int J Solids Struct 41(22-23):6291–6315
63. Landis CM (2004) Non-linear constitutive modeling of ferroelectrics. Curr Opin Solid State Mater Sci 8:59–69
64. Li Q, Kuna M (2012) Evaluation of electromechanical fracture behavior by configurational forces in cracked ferroelectric polycrystals. Comput Mater Sci 57:94–101
65. Li W, Landis CM (2011) Nucleation and growth of domains near crack tips in single crystal ferroelectrics. Eng Fract Mech 78(7):1505–1513
66. Li WY, McMeeking RM, Landis CM (2008) On the crack face boundary conditions in electromechanical fracture and an experimental protocol for determining energy release rates. Eur J Mech A-Solids 27(3):285–301
67. Li XF, Tang GJ (2003) Electroelastic analysis for a piezoelectric layer with surface electrodes. Mech Research Commun 30:345–351
68. Li YL, Cross LE, Chen LQ (2005) A phenomenological thermodynamic potential for BaTiO3 single crystals. J Appl Phys 98:064,101
69. Linder C, Miehe C (2012) Effect of electric displacement saturation on the hysteretic behavior of ferroelectric ceramics and the initiation and propagation of cracks in piezoelectric ceramics. J Mech Phys Solids 60:882–903
70. Lines M, Glass A (1979) Principles and applications of ferroelectrics and related materials. Clarendon Press
71. Liu TQ, Oates WS, Wan S, Lynch CS (2005) Crack initiation at electrode edges in PZN-4.5PT single crystals. J Intell Mater Syst Struct 16:373–379
72. Lucato SLDE, Lupascu DC, Kamlah M, Rodel J, Lynch CS (2001) Constraint-induced crack initiation at electrode edges in piezoelectric ceramics. Acta Mater 49:2751–2759
73. Lucato SLDE, Bahr HA, Pham VB, Lupascu DC, Balke H, Rodel J, Bahr U (2002) Electrically driven cracks in piezoelectric ceramics: experiments and fracture mechanics analysis. J Mech Phys Solids 50:2333–2353
74. Lucato SLDE, Bahr HA, Pham VB, Lupascu DC, Balke H, Rodel J, Bahr U (2003) Crack deflection in piezoelectric ceramics. J Eur Ceram Soc 23:1147–1156
75. Lynch CS (1998) Fracture of ferroelectric and relaxor electro-ceramics: Influence of electric field. Acta Mater 46(2):599–608
76. Lynch CS, Chen L, Suo Z, McMeeking RM, Yang W (1995) Crack-growth in ferroelectric ceramics driven by cyclic polarization switching. J Intell Mater Syst Struct 6:191–198
77. McMeeking RM (1999) Crack tip energy release rate for a piezoelectric compact tension specimen. Eng Fract Mech 64(2):217–244
78. McMeeking RM (2004) The energy release rate for a griffith crack in a piezoelectric material. Eng Fract Mech 71(7-8):1149–1163
79. McMeeking RM, Landis CM (2002) A phenomenological multi-axial constitutive law for switching in polycrystalline ferroelectric ceramics. Int J Eng Sci 40(14):1553–1577
80. Meschke F, Kolleck A, Schneider GA (1997) R-curve behaviour of BaTiO3 due to stress-induced ferroelastic domain switching. J Am Ceram Soc 17(9):1143–1149
81. Meschke F, Raddatz O, Kolleck A, Schneider GA (2000) R-curve behavior and crack-closure stresses in barium titanate and (Mg,Y)-PSZ ceramics. J Am Ceram Soc 83(2):353–361
82. Miehe C, Welschinger F, Hofacker M (2010) A phase field model of electromechanical fracture. J Mech Phys Solids 58(10):1716–1740
83. Miehe C, Welschinger F, Hofacker M (2010) Thermodynamically consistent phase-field models of fracture: Variational principles and multi-field FE implementations. Int J Numer Methods Eng 83(10):1273–1311
84. Moes N, Dolbow J, Belytschko T (1999) A finite element method for crack growth without remeshing. Int J Numer Methods Eng 46(1):131–150
85. Oliver J, Huespe AE, Pulido MDG, Chaves E (2002) From continuum mechanics to fracture mechanics: the strong discontinuity approach. Eng Fract Mech 69(2):113–136
86. Park SB, Sun CT (1995) Fracture criteria for piezoelectric ceramics. J Am Ceram Soc 78(6):1475–1480
87. Parton VZ (1976) Fracture mechanics of piezoelectric materials. Acta Astronautica 3(9-10):671–683
88. Peco C, Rosolen A, Arroyo M (2013) An adaptive meshfree method for phase-field models of biomembranes. part *ii*: A lagrangian approach for membranes in viscous fluids. J Comput Phys 249:320–336
89. Pisarenko GG, Chushko VM, Kovalev SP (1985) Anisotropy of fracture toughness of piezoelectric ceramics. J Am Ceram Soc 68(5):259–265
90. Pojprapai S, Jones LJ, Vodenitcharova T, Bernier JV, Hoffman M (2011) Investigation of the domain switching zone near a crack tip in pre-poled

lead zirconate titanate ceramic via in situ X-ray diffraction. Scripta Mater 64(1):1–4
91. Pritchard J, Bowen CR, Lowrie F (2001) Multilayer actuators: review. Brit Ceram Trans 100:265–273
92. Qian TY, Tong CF, Zhang P (1998) Linear electro-elastic analysis of a cavity or a crack in a piezoelectric material. Int J Solids Struct 35(17):2121–2149
93. Rajapakse RKND, Zeng X (2001) Toughening of conducting cracks due to domain switching. Acta Mater 49:877–885
94. Ratz A, Ribalta A, Voigt A (2006) Surface evolution of elastically stressed films under deposition by a diffuse interface model. J Comput Phys 214(1):187–208
95. Ricoeur A, Kuna M (2003) Influence of electric fields on the fracture of ferroelectric ceramics. J Eur Ceram Soc 23(8):1313–1328
96. Rosato C, Miehe D, Linder C (2011) New finite elements with embedded strong discontinuities for the modeling of failure in electromechanical coupled solids. Comput Methods Appl Mech Eng 200(1-4):141–161
97. Rosolen A, Peco C, Arroyo M (2013) An adaptive meshfree method for phase-field models of biomembranes. part *i*: Approximation with maximum-entropy basis functions. J Comput Phys DOI: http://dx.doi.org/10.1016/j.jcp.2013.04.046
98. Ru CQ (2000) Exact solution for finite electrode layers embedded at the interface of two piezoelectric half-planes. J Mech Phys Solids 48:693–708
99. Ru CQ, Mao X, Epstein M (1998) Electric-field induced interfacial cracking in multilayer electrostrictive actuators. J Mech Phys Solids 46:1301–1318
100. Schneider GA (2007) Influence of electric field and mechanical stresses on the fracture of ferroelectrics. Annu Rev Mater Res 37:491–538
101. Schneider GA, Heyer V (1999) Influence of the electric field on vickers indentation crack growth in BaTiO3. J Eur Ceram Soc 19(6-7):1299–1306
102. Schrade D, Mueller R, Xu BX, Gross D (2007) Domain evolution in ferroelectric materials: A continuum phase field model and finite element implementation. Comput Methods Appl Mech Eng 196(41-44):4365–4374
103. Sekerka RF (2004) Morphology: from sharp interface to phase field models. J Cryst Growth 264(4):530–540
104. Sheng JS, Landis CM (2007) Toughening due to domain switching in single crystal ferroelectric materials. Int J Fract 143(2):161–175
105. Shieh J, Huber JE, Fleck NA (2006) Fatigue crack growth in ferroelectrics under electrical loading. J Eur Ceram Soc 26:95–109
106. Shindo Y, Murakami H, Horiguchi K, Narita F (2002) Evaluation of electric fracture properties of piezoelectric ceramics using the finite element and single-edge precracked-beam methods. J Am Ceram Soc 85(5):1243–1248
107. Shu YC, Bhattacharya K (2001) Domain patterns and macroscopic behaviour of ferroelectric materials. Philos Mag B 81(12):2021–2054
108. Song YC, Soh AK, Ni Y (2007) Phase field simulation of crack tip domain switching in ferroelectrics. J Phys D: Appl Phys 40(4):1175–1182
109. Steinbach I (2009) Phase-field models in materials science. Model Simul Mater Sci Eng 17(7)
110. Su Y, Landis CM (2007) Continuum thermodynamics of ferroelectric domain evolution: Theory, finite element implementation, and application to domain wall pinning. J Mech Phys Solids 55(2):280–305
111. Sukumar N, Srolovitz DJ, Baker TJ, Prevost JH (2003) Brittle fracture in polycrystalline microstructures with the extended finite element method. Int J Numer Methods Eng 56:2015–2037
112. Sun CT, Park SB (2000) Measuring fracture toughness of piezoceramics by vickers indentation under the influence of electric fields. Ferroelectrics 248(1-4):79–95
113. Suo Z (1991) Mechanics concepts for failure in ferroelectric ceramics. Amer Soc Mech Eng 24:1–6
114. Suo Z (1993) Models for breakdown-resistant dielectric and ferroelectric ceramics. J Mech Phys Solids 41:1155–1176
115. Tieresten HF (1969) Linear piezoelectric plate vibrations. Plenum Press
116. Tobin AG, Pak YE (1993) Effects of electric fields on fracture behavior of pzt ceramics. Proc SPIE Smart Struct Mater 1916:78–86
117. Uchino K, Furuta A (1992) Destruction mechanism of multilayer ceramic actuators. In: M Liu and A Safari and A Kingon And G Haertling (ed) ISAF 92 : Proc. 8th IEEE Int. Symp. Applications of Ferroelectrics, pp 195–198
118. Uchino K, Takahashi S (1996) Multilayer ceramic actuators. Curr Opin Solid State Mater Sci 1:698–705
119. Vendik OG, Zubko SP (2000) Ferroelectric phase transition and maximum dielectric permittivity of displacement type ferroelectrics ($Ba_xSr_{1-x}TiO_3$). J Appl Phys 88:5343–5350

120. Verhoosel CV, Gutierrez MA (2009) Modelling inter- and transgranular fracture in piezoelectric polycrystals. Eng Fract Mech 76(6):742–760
121. Wang HY, Singh RN (1997) Crack propagation in piezoelectric ceramics: Effects of applied electric fields. J Appl Phys 81(11):7471–7479
122. Wang J, Kamlah M (2009) Three-dimensional finite element modeling of polarization switching in a ferroelectric single domain with an impermeable notch. Smart Mater Struct 18:104,008
123. Wang J, Kamlah M (2010) Effect of electrical boundary conditions on the polarization distribution around a crack embedded in a ferroelectric single domain. Eng Fract Mech 77(18):3658–3669
124. Wang J, Landis CM (2006) Effects of in-plane electric fields on the toughening behavior of ferroelectric ceramics. J Mech Mater Struct 1(6):1075–1095
125. Wang J, Zhang TY (2007) Phase field simulations of polarization switching-induced toughening in ferroelectric ceramics. Acta Mater 55(7):2465–2477
126. Wang X (2005) Phase field models and simulations of vesicle bio-membranes. PhD thesis, Pennsylvania State University
127. Wang YL, Tagantsev AK, Damjanovic D, Setter N, Yarmarkin VK, Sokolov AI, Lukyanchuk IA (2007) Landau thermodynamic potential for BaTiO3. J Appl Phys 101:104,115
128. Westrain I, Oates WS, Lupascu DC, Roedel J, Lynch CS (2007) Mechanism of electric fatigue crack growth in lead zirconate titanate. Acta Mater 55:301–312
129. Westram I, Lupascu D, Roedel J, Laskewitz B, Kamlah M (2007) Electric-field-induced crack initiation from a notch in a ferroelectric ceramic. J Am Ceram Soc 90:2849–2854
130. Wilson ZA, Borden MJ, Landis CM (2013) A phase-field model for fracture in piezoelectric ceramics. Int J Fract DOI 10.1007/s10704-013-9881-9
131. Winzer SR, Shankar N, Ritter AP (1989) Designing cofired multilayer electrostrictive actuators for reliability. J Am Ceram Soc 72:2246–2257
132. Xu BX, Schrade D, Mueller R, Gross D (2009) Micromechanical analysis of ferroelectric structures by a phase field method. Comput Mater Sci 45(3):832–836
133. Xu BX, Schrade D, Gross D, Mueller R (2010) Phase field simulation of domain structures in cracked ferroelectrics. Int J Fract 165:163–173
134. Xu XP, Needleman A (1994) Numerical simulations of fast crack-growth in brittle solids. J Mech Phys Solids 42(9):1397–1434
135. Yang L, Dayal K (2011) Effect of lattice orientation, surface modulation, and applied fields on free-surface domain structure in ferroelectrics. Acta Mater 59(17):6594–6603
136. Yang L, Dayal K (2012) Microstructure and stray electric fields at surface cracks in ferroelectrics. Int J Fract 174:17–27
137. Yang W, Suo Z (1994) Cracking In Ceramic Actuators Caused By Electrostriction. J Mech Phys Solids 42:649–663
138. Yang W, Zhu T (1998) Switch-toughening of ferroelectrics subjected to electric fields. J Mech Phys Solids 46(2):291–311
139. Ye RQ, He LH (2001) Electric field and stresses concentrations at the edge of parallel electrodes in piezoelectric ceramics. Int J Solids Struct 38:6941–6951
140. Zhang TY, Gao CF (2004) Fracture behaviors of piezoelectric materials. Theor Appl Fract Mech 41(1-3):339–379
141. Zhang TY, Wang TH, Zhao MH (2003) Failure behavior and failure criterion of conductive cracks (deep notches) in thermally depoled PZT-4 ceramics. Acta Mater 51(16):4881–4895
142. Zhang TY, Liu GN, Wang Y (2004) Failure behavior and failure criterion of conductive cracks (deep notches) in piezoelectric ceramics II: experimental verification. Acta Mater 52:2025–2035
143. Zhang TY, Liu G, Wang T, Tong P (2007) Application of the concepts of fracture mechanics to the failure of conductive cracks in piezoelectric ceramics. Eng Fract Mechanics 74(7):1160–1173
144. Zhang W, Bhattacharya K (2005) A computational model of ferroelectric domains. part *i*: model formulation and domain switching. Acta Mater 53(1):185–198
145. Zhang W, Bhattacharya K (2005) A computational model of ferroelectric domains. part *ii*: grain boundaries and defect pinning. Acta Mater 53(1):199–209
146. Zhao XJ, Liu B, Fang DN (2010) Study on electroelastic field concentration around the electrode tip in multilayer ferroelectric actuators of two designs and their optimizations. Int J Plast 26:533–548
147. Zhu T, Yang W (1997) Toughness variation of ferroelectrics by polarization switch under nonuniform electric field. Acta Mater 45(11):4695–4702
148. Zhu T, Yang W (1999) Fatigue crack growth in ferroelectrics driven by cyclic electric loading. J Mech Phys Solids 47(1):81–97